Exploring Structural Sparsity of Coil Images from 3-Dimensional Directional Tight Framelets for SENSE Reconstruction*

Yan-Ran Li, Raymond H. F. Chan, Lixin Shen, Xiaosheng Zhuang, Risheng Wu, Yijun Huang, Junwei Liu†

Abstract. Each coil image in a parallel magnetic resonance imaging (pMRI) system is an imaging slice modulated by the corresponding coil sensitivity. These coil images, structurally similar to each other, are stacked together as a 3-dimensional (3D) image data and their sparsity property can be explored via 3D directional Haar tight framelets. The features of the 3D image data from the 3D framelet systems are utilized to regularize sensitivity encoding (SENSE) pMRI reconstruction. Accordingly, a so-called SENSE3d-algorithm is proposed to reconstruct images of high quality from the sampled K-space data with a high acceleration rate by decoupling effects of the desired image (slice) and sensitivity maps. Since both the imaging slice and sensitivity maps are unknown, this algorithm repeatedly performs a slice-step followed by a sensitivity-step by using updated estimations of the desired image and the sensitivity maps. In the slice-step, for the given sensitivity maps, the estimation of the desired image is viewed as the solution to a convex optimization problem regularized by the sparsity of its 3D framelet coefficients of coil images. This optimization problem, involved data from the complex field, is solved by a primal-dual-three-operator splitting (PD3O) method. In the sensitivity-step, the estimation of sensitivity maps is modelled as the solution to a Tikhonov-type optimization problem that favours the smoothness of the sensitivity maps. This corresponding problem is nonconvex, and could be solved by a forward-backward splitting method. Experiments on real phantoms and in-vivo data show that the proposed SENSE3d-algorithm can explore the sparsity property of the imaging slices and efficiently produce reconstructed images of high quality with reducing aliasing artifacts caused by high acceleration rate, additive noise, as well as the inaccurate estimation of each coil sensitivity. To provide a comprehensive picture of the overall performance of our SENSE3d model, we provide quantitative index (HaarPSI) and comparisons to some deep learning methods such as VarNet and fastMRI-UNet.

Key words. pMRI and SENSE, Structural sparsity, Directional Haar framelet regularization, 3D features, PD3O, HaarPSI, U-Net, VarNet, fastMRI-UNet.

AMS subject classifications. 42C15, 42C40, 58C35, 65D18, 65D32

1. Introduction and motivation.

The Magnetic Resonance Imaging (MRI) is a common technique in medical diagnosis. Most of the MRI sequences in use today are based on a "spin-warp" imaging scheme [7], where the spatial information with phase was encoded successively by varying the amplitude of the gradients of the radio frequency pulses. Such a scheme is a Fourier-transform MRI

*Submitted to editors DATE.

Funding: The work of R. Chan was supported in part by HKRGC Grants Nos. CUHK14301718, NCityU214/19, CityU11301120, CityU11309922, C1013-21GF, and CityUGrant9380101. The work of L. Shen was supported in part by the National Science Foundation under grant DMS-1913039 and DMS-2208385, and Syracuse CUSE grant. The work of X. Zhuang was supported in part by the Research Grants Council of Hong Kong (Project no. CityU 11302218) and City University of Hong Kong (Project no. 7005603).

†Y.-R. Li, R. Wu, Y. Huang and J. Liu are with College of Computer Science and Software Engineering, Shenzhen University, Shenzhen, 518060, China, Emails: lyran@szu.edu.cn, sunrise_wu@foxmail.com, 2070276106@email.szu.edu.cn, 2200271023@email.szu.edu.cn; L. Shen is with Department of Mathematics, Syracuse University, Syracuse, NY 13244, Email: lshen03@syr.edu; R. Chan is with Department of Mathematics, City University of Hong Kong, Tat Chee Avenue, Kowloon Tong, Hong Kong SAR,China; Hong Kong Centre for Cerebro-Cardiovascular Health Engineering, Email:raymond.chan@cityu.edu.hk; X. Zhuang is with Department of Mathematics, City University of Hong Kong, Tat Chee Avenue, Kowloon Tong, Hong Kong, Emails: xzhuang7@cityu.edu.hk.

method that produces data in the spatial frequency space, known as the *K-space*. The spatial frequency domain content of the imaged object is encoded directly into $g(k_x, k_y)$, the magnetic resonance (MR) signal at spatial frequencies k_x and k_y in the x- and y-directions, respectively. In the *K*-space of the form $g(k_x, k_y) = \iint s(x, y)u(x, y)e^{2\pi i x k_x} e^{2\pi i y k_y} dxdy$, where $s(x, y)$ is the *coil sensitivity function* and $u(x, y)$ is the *spatial spin density function* of the original object such as bones, joints, and soft tissues. The decoding process involves the inverse Fourier transform to obtain the target MRI image $u(x, y)$ for medical diagnosis purpose. In order to reproduce accurate reconstruction images, enough phase-encoding steps are needed to cover sufficient positions in the *K*-space. Hence, the MRI scans typically take longer time.

Parallel MRI (pMRI) technique is a hardware solution used in clinical applications to shorten the imaging time. It utilizes a set of receiver coils surrounding the target object to detect the MR signals. To accelerate the data acquisition procedure, the pMRI system uses reconstruction algorithms to predict the imaging structures of the original MR signal only from collected partial (downsampling) *K*-space data [9, 28]. This downsampling process significantly reduces the scan time, but the resulting pMRI reconstruction is ill-posed and requires regularization techniques to improve the quality of the MRI images [6]. Most pMRI techniques can be categorized as the image domain methods (e.g., SENSE), the *K*-space methods (e.g., GRAPPA), and their hybrids. In this paper, we focus on the SENSE-based pMRI method.

1.1. SENSE-based pMRI reconstruction. SENSE is a technique that allows a reduction in scan time through the use of multiple receiver coils in an imaging mode [28]. More precisely, in a pMRI process, we denote g_ℓ the acquired *K*-space signal received by the ℓth coil by

$$g_\ell = PF(s_\ell \odot u) + \eta_\ell, \quad \ell = 1, \ldots, L, \tag{1.1}$$

where L is the total number of coils, $u \in \mathbb{R}^n$ is the vectorization form of the desired image representing the density of the hydrogen protons in tissues (this is for convenience of presentation, in practice, u is kept as a 2D image), $F \in \mathbb{C}^{n\times n}$ is the discrete Fourier transform matrix, $P \in \mathbb{R}^{n\times n}$ is a sampling matrix, $\eta_\ell \in \mathbb{C}^n$ is the additive noise, and $s_\ell \in \mathbb{C}^n$ is the sensitivity vector of the ℓth coil. Here, $a \odot b$ is the Hadamard product of a and b with the same dimension. The sampling matrix P is diagonal with diagonal entries being 0 or 1. The observation model in (1.1) shows that the coils simultaneously measure the same region but with downsampling process in order to increase the scan speed.

When the sensitivity vectors s_ℓ are available, we can write (1.1) in a compact form. To this end, let us define $S_\ell := \mathrm{diag}(s_\ell)$ for $\ell = 1, \ldots, L$ and

$$g := \begin{bmatrix} g_1 \\ \vdots \\ g_L \end{bmatrix}, S := \begin{bmatrix} S_1 \\ \vdots \\ S_L \end{bmatrix}, \eta := \begin{bmatrix} \eta_1 \\ \vdots \\ \eta_L \end{bmatrix}, M := \begin{bmatrix} PFS_1 \\ \vdots \\ PFS_L \end{bmatrix}. \tag{1.2}$$

With these notation, a unified representation of the acquired signal g_ℓ in equation (1.1) is given by

$$g = Mu + \eta, \tag{1.3}$$

where $g \in \mathbb{C}^{Ln}$, $M \in \mathbb{C}^{Ln\times n}$, and $\eta \in \mathbb{C}^{Ln}$.

Regularization techniques are often adopted to regularize the ill-posed problem (1.3). In what follows, we address the issues related to dealing with the inverse problem (1.3).

1.2. Structural sparsity of coil images explored via 3D directional framelets. Regularization techniques on the 2D target image are commonly used for the SENSE methods to improve the reconstruction quality. One typical example is the framelet (or wavelet) regularization model of the form:

$$\min\left\{\frac{1}{2}\|Mu-g\|_2^2+\|\Gamma W_{2D}u\|_1 : u\in\mathbb{R}^n\right\}, \tag{1.4}$$

where Γ is a diagonal matrix with non-negative diagonal elements, and W_{2D} is the matrix associated with a 2D framelet transform. Model (1.4) uses fixed (pre-estimated) coil sensitivity maps s_ℓ and regularizes on the framelet coefficients of the underlying target image u. It applies W_{2D} on each coil image or target slice to produce sparse coefficient sequences, and process them one by one. We refer to (1.4) as *SENSE2d-U model*.

The pMRI system has multiple coil images and each coil image containing parts of the information of the target slice which are correlated with each others. For example, Fig. 1(a) shows the four coil images of size $512\times$ 512 from (the inverse discrete Fourier transform of) the corresponding full *K*-space data g_ℓ acquired by an MRI machine. It can be seen that the intensity of each coil image is uneven and the intensities of the coil images are mismatched. Without considering their correlated information together, it could lead to poor quality of the reconstruction image, e.g., see Fig. 2(c).

Observe that the coil images are sparse in two aspects: (1) each coil image contains essentially smooth areas separated by edge features, and (2) the coil images are structurally similar to each others with areas of different high intensity. How can we explore the sparsity within each coil image and among different coil images? In view of the fact that the coil images are from the same target slice modulated via multiple coils in different positions, it is thus natural and reasonable to stack and view them as a 3D signal (data) of size $512\times512\times4$, see Fig. 1(b). We can then use a 3D directional framelet system to get a more harmonic image and explore its sparsity. More precisely, using a 3D Haar lowpass filter a^H in a 3D directional framelet system $\mathrm{DHF}_3^3=\{a^H; b_x, b_y, b_{xy}, b_{x,y}, b_{aux}\}$ (see Section 2), which plays the role of averaging, the neighbouring coil images with labels (1) – (4) are averaged, which produces a 3D signal of four images, labelled as $(1+2)$, $(2+3)$, $(3+4)$, and $(4+1)$, having more areas with less intensive difference, see Fig. 1(c). In the second level, the 3D signal, which is the stacked version of the four images $(1+2)$, $(2+3)$, $(3+4)$, and $(4+1)$, is further averaged by the upsampled lowpass filter, which produces a 3D signal of four images with label $(1+2+3+4)$ having almost the same intensity level of brightness (see Fig. 1(d)). The lowpass filtering by the 3D tight framelet filter greatly utilizes the correlated information among the coil images as well within the coil images to produce images with harmonic intensity level, which in turn facilitates the production of the sparse representation of the 3D signal by the directional high-pass filters $b_x, b_y, b_{xy}, b_{x,y}$ (playing the role of differencing) of the 3D framelet system DHF_3^3. The full 3D directional framelet system DHF_3^3 plays the central role in our 3D SENSE-based pMRI regularization model.

In view of the above discussion, it is natural to consider the following 3D framelet regularization pMRI model:

$$\min\left\{\frac{1}{2}\|Mu-g\|_2^2+\|\Gamma W_{3D}Su\|_1 : u\in\mathbb{R}^n\right\}, \tag{1.5}$$

where W_{3D} is the matrix associated with a 3D tight framelet transform. The differences of the regularization terms in (1.4) and (1.5) are obvious. The regularization term $\|\Gamma W_{2D}u\|_1$ in (1.4) measures

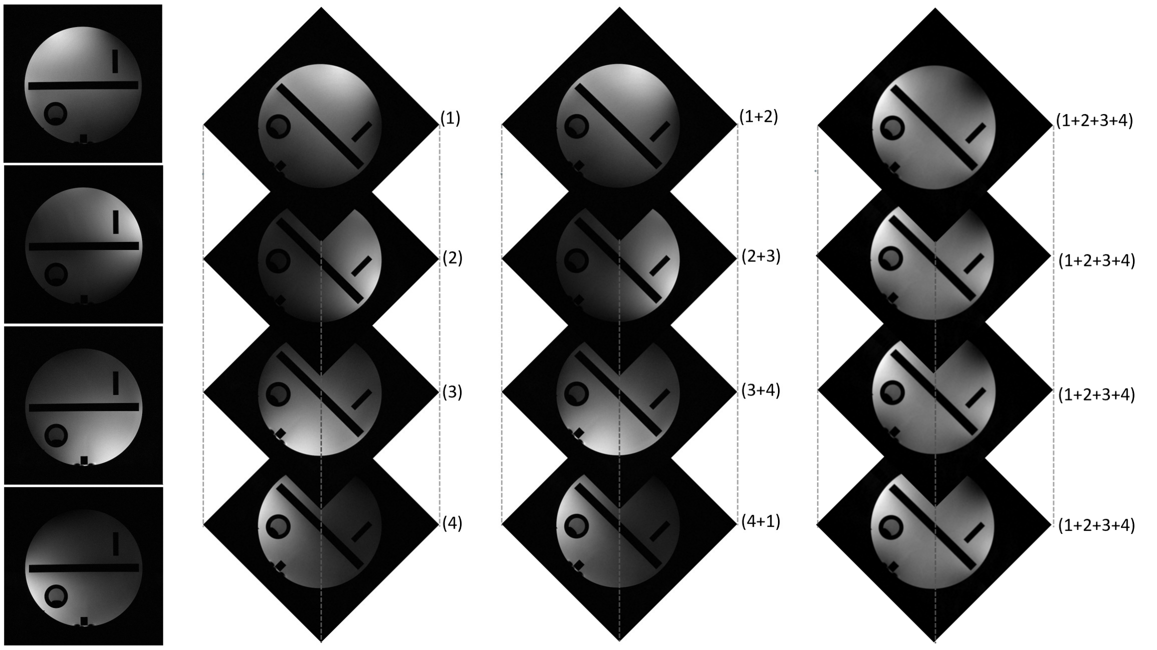

(a) coil img. (b) 3D data (c) 1^{st} level (d) 2^{nd} level

Figure 1. *2-Level 3D directional Haar tight framelet lowpass filtering. (a) Four 512×512 coil images. (b) The 4 coil images, labeled as (1), (2), (3), and (4), are stacked as a 3D image data of size $512 \times 512 \times 4$. (c) First level lowpass filtering of the 3D image by a 3D Haar lowpass filter a^H. This results in images obtained from averaging within each coil image and across coil images. (d) Second level low-pass filtering of the middle 3D image. Each slice of the second level filtered 3D image is the same, which is the average of the 4 coil images.*

the sparsity with the ℓ_1 norm for the desired image u under a 2D tight framelet transform while the regularization term $\|\Gamma W_{3D} S u\|_1$ in (1.5), as motivated by Fig. 1(c), measures the sparsity with the ℓ_1 norm of *all* coil images Su under a 3D framelet transform. If S is pre-estimated, then we shall call such a model in (1.5) the *SENSE3d-U model*.

1.3. The SENSE3d-algorithm and the SENSE3d model.

The sensitivity vectors s_ℓ are spatially nonuniform and are unknown. The difficulty of model (1.5) is to find an estimate of u under the scenario that s_ℓ are unknown and the acquired K-space signals g_ℓ are incomplete. For the SENSE2d-U model and SENSE3d-U models, each sensitivity map s_ℓ is usually pre-estimated as follows: the blurry coil image $\tilde{g}_\ell = F^{-1} g_\ell$ is acquired by the inverse Fourier transform of the center K-space data, and then the sensitivity for each coil is estimated as $s_\ell = \tilde{g}_\ell / \sqrt{|\tilde{g}_1|^2 + \cdots + |\tilde{g}_L|^2}$. However, both models with such pre-estimated coil selectivity maps usually do not perform well. See Figs. 2(c) and (d).

We treat both u and the sensitivity vectors s_ℓ as our *target solutions* in our proposed optimization models and propose a so-called SENSE3d-algorithm to find the estimates of u and s_ℓ iteratively. The basic steps in the SENSE3d-algorithm are the 'Slice-step' and the 'Sensitivity-step':

(1) Slice-step: Find an estimate of the slice image u from the observed K-space signals g_ℓ and the guesses of s_ℓ. The reconstruction of u from (1.3) is obtained by solving an optimization

model (see (1.5) or (3.3)) regularized by a 3D directional Haar tight framelet system.

(2) Sensitivity-step: Update the sensitivity vectors s_ℓ, for $\ell = 1, 2, \ldots, L$, from the observed K-space signal g_ℓ and the estimate of u. The target image u is obtained by using a smooth assumption on s_ℓ. Once we have an approximation to the target image u, we can use it to update the sensitivities that are the solution of a Tikhonov-type optimization model (see (3.10)).

The above two steps are alternately repeated until stability is reached. To avoid additional notation, details on the 'Slice-step' and the 'Sensitivity-step' will be discussed in Section 3. We shall call the model using the SENSE3d-algorithm, that is (3.3)+(3.10) detailed in Section 3, together with our DHF_3^3 framelet regularization, the *SENSE3d model*.

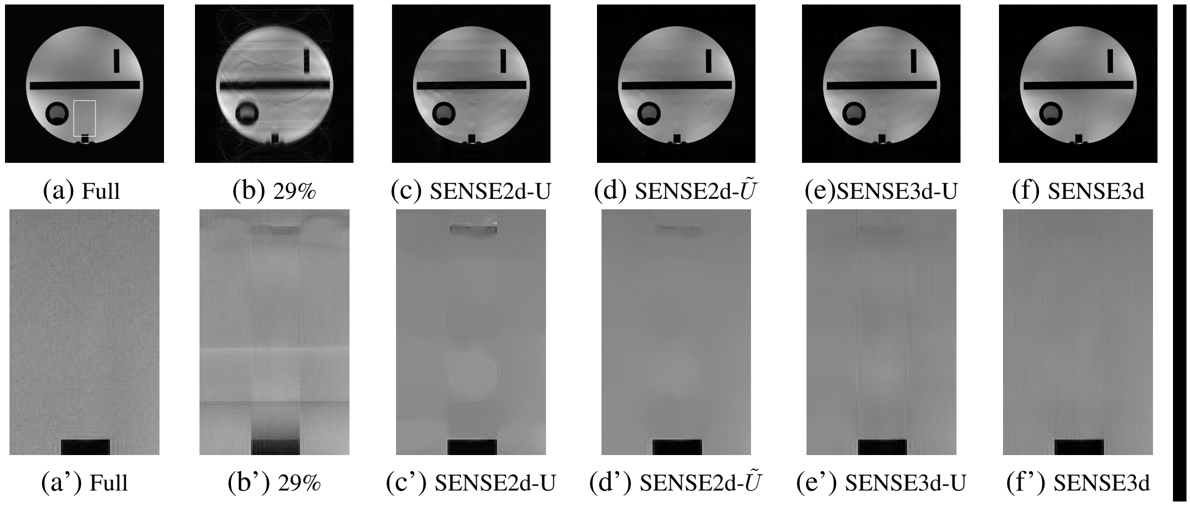

Figure 2. *(a) Reference SoS image by the full K-space data with to-be zoom-in area (the white rectangle); (b) SoS image by the four coil images with 29% K-space data on uniform sampling model as shown in Fig. 3(a); (c) The* SENSE2d-U *model* (1.4) *by pMRI algorithm FADHFA [21]; (d) The* SENSE2d-$\tilde{U}$ *which is the pMRI algorithm FADHFA using the sensitivity map estimated by our SENSE3d algorithm; (e) The* SENSE3d-U *model* (1.5)*; and (f) The* SENSE3d *model* (3.3)+(3.10)*. (a')–(f'): The zoom-in part of (a)–(f) of the same white rectangle area, respectively.*

The *SENSE3d* model significantly improves the quality of the reconstruction target image u. One can see the performance comparisons among the three models *SENSE2d-U*, *SENSE3d-U*, *SENSE3d*, and *SENSE2d-*$\tilde{U}$, from Fig. 2. We use the phantom images with four coil images of size 512×512. The K-space data of each coil is partially sampled according to the sampling model in Fig. 3(a) (29% of the K-space with 24 auto calibration signal (ACS) lines). Fig. 2(b) is the SoS (sum-of-square) image of the four downsampled coil images, which is obviously blurred with aliasing artifacts. The MRI images reconstructed by *SENSE2d-U*, *SENSE2d-*$\tilde{U}$, *SENSE3d-U*, and *SENSE3d* are shown in Figs. 2(c), (d), (e), and (f), respectively.

Comparing *SENSE3d-U* and *SENSE2d-U* model, one can see that *SENSE3d-U* model is better in reducing the aliasing artifacts than that of *SENSE2d-U* model. As shown by the zoom-in parts, the "Column" and the "Row" aliasing artifacts in Fig. 2(c') (*SENSE2d-U*) are mostly reduced by the *SENSE3d-U* model in Fig. 2(e'). This confirms that the correlated futures of coil images by our 3D framelet system can efficiently suppress the artifacts by the downsamping operation in the K-space domain. Comparing the *SENSE3d-U* model (without iterating updating of s_ℓ) and the *SENSE3d* model (with iterating updating of s_ℓ), one can see from Figs. 2(e) and (f) that the reconstruction target image u by the *SENSE3d* does not have aliasing artifacts. The zoom-in parts in Figs. 2(e') and (f') show that the *SENSE3d* model can get more accurate sensitivity to reconstruct better target images. Aliasing artifacts in Fig. 2(e') are removed in Fig. 2(f') via our *SENSE3d* models. Finally, the *SENSE2d-$\tilde{U}$*, which is the pMRI algorithm FADHFA using the sensitivity map estimated by our SENSE3d algorithm, shows its improvement over *SENSE2d-U*, but it is still not as good as *SENSE3d-U*.

The performance of the *SENSE3d-U* model from the above is better than that of the *SENSE2d-U* model while the performance of *SENSE3d* model is better than that of the *SENSE3d-U* model. The reconstructed and sensitivity models in (3.3) and (3.10), respectively, are interacted with each other to improve the quality of the MRI images by our DHF_3^3 framelet regularization. We demonstrate in Section 4 with more experimental results for comparing with other state-of-the-art methods.

1.4. Contributions and structure.

The contributions of the paper mainly lie in the following three aspects. First, we introduce the use of 3D directional Haar framelets for the regularization of the pMRI reconstruction under the SENSE-based method. In view of the correlated information among coil images, the 3D directional Haar framelet system DHF_3^3 not only produces coil images with harmonic pixel intensity but also greatly facilitates the exploration of the sparsity within each coil image as well as the sparsity across coil images. Secondly, we propose a so-called *SENSE3d*-algorithm to estimate the target image and the coil sensitivity maps iteratively. Unlike some 2D models and 3D models that are using pre-estimated coil sensitivity maps, our *SENSE3d*-algorithm treats both the underlying image u and the coil sensitivity maps s_ℓ as our target solutions of some optimization models by 3D regularization. Such a *SENSE3d*-algorithm together with our 3D directional Haar framelet regularization gives rise to our *SENSE3d* model, which provides high quality reconstruction images with excellent performance improvement. Finally, we provide detailed step-by-step procedures for solving the optimization problems appeared in the Slice-step and Sensitivity-step of the *SENSE3d*-algorithm. Moreover, we gives theoretical justifications on the convergence analysis of the two iterative algorithms for the Slice-step and Sensitivity-step, respectively.

The structure of the paper is as follows. In Section 2, we discuss 3D directional Haar framelets for our pMRI regularization. In Section 3, we present our optimization model for the pMRI SENSE reconstruction and develop the numerical algorithms to solve the model iteratively. In Section 4, we conduct numerical experiments on the comparisons of several state-of-the-art methods using various MRI data. Conclusions and further remarks are given in the last section. Some proofs are postponed to the appendix.

2. 3-Dimensional directional Haar framelets filter banks.

In what follow, we briefly discuss the 3D directional Haar tight framelet filter bank DHF_3^3 for our 3D SENSE-based pMRI regularization model.

By $l_0(\mathbb{Z}^d)$ we denote the set of all finitely supported sequences. A *mask/filter* $h = \{h(k)\}_{k\in\mathbb{Z}^d} : \mathbb{Z}^d \to \mathbb{C}$ on $\mathbb{Z}^d$ is a sequence in $l_0(\mathbb{Z}^d)$ whose *Fourier series* is defined to be $\widehat{h}(\xi) := \sum_{k\in\mathbb{Z}^d} h(k)e^{-ik\cdot\xi}$ for $\xi \in \mathbb{R}^d$. We denote $\boldsymbol{\delta}$ as the *the Dirac sequence* such that $\boldsymbol{\delta}(0) = 1$ and $\boldsymbol{\delta}(k) = 0$ for all $k \in \mathbb{Z}^d\backslash\{0\}$, and $\boldsymbol{\delta}_\gamma := \boldsymbol{\delta}(\cdot - \gamma)$ for $\gamma \in \mathbb{Z}^d$. Throughout the paper, we assume the tight framelets are *dyadic dilated*, that is, the *dilation matrix* is $2I_d$ with I_d the $d \times d$ identity matrix. For filters $a, b_1, \ldots, b_m \in l_0(\mathbb{Z}^d)$, we say that a filter bank $\{a; b_1, \ldots, b_m\}$ is *a (d-dimension dyadic) tight* *framelet filter bank* if $\forall\, \xi \in \mathbb{R}^d, \omega \in \{0,1\}^d$,

$$\widehat{a}(\xi)\overline{\widehat{a}(\xi+\pi\omega)} + \sum_{\iota=1}^{m} \widehat{b_\iota}(\xi)\overline{\widehat{b_\iota}(\xi+\pi\omega)} = \boldsymbol{\delta}(\omega), \tag{2.1}$$

where $\bar{x}$ denotes the complex conjugate of $x \in \mathbb{C}$. The filter a is a *lowpass filter* satisfying $\widehat{a}(0) = 1$ while b_ι's are the *highpass filters* satisfying $\widehat{b_\iota}(0) = 0$. Such a filter bank $\{a; b_1, \ldots, b_m\}$ corresponds to a *framelet system* $\{\varphi; \psi_1, \ldots, \psi_m\}$ through the refinement relations: $\widehat{\varphi}(2\xi) = \widehat{a}(\xi)\widehat{\varphi}(\xi)$ and $\widehat{\psi_\iota}(2\xi) = \widehat{b_\iota}(\xi)\widehat{\varphi}(\xi)$, where the *Fourier transform* is defined to be $\widehat{f}(\xi) := \int_{\mathbb{R}^d} f(x)e^{-ix\cdot\xi}dx$ for a function $f \in L_1(\mathbb{R}^d)$. For more details, we refer to [11].

Now consider $a^H = 2^{-d}\sum_{\gamma\in\{0,1\}^d} \boldsymbol{\delta}_\gamma$ to be the d-dimensional Haar lowpass filter. Define the set $\{b_1, \ldots, b_m\} := \{2^{-d}(\boldsymbol{\delta}_{\gamma_1} - \boldsymbol{\delta}_{\gamma_2}) : \gamma_1, \gamma_2 \in \{0,1\}^d \text{ and } \gamma_1 < \gamma_2\}$ of highpass filters. Here $\gamma_1 < \gamma_2$ is understood in the sense of lexicographical order. Then we have $m = \binom{2^d}{2} = 2^{d-1}(2^d - 1)$. It was shown in [12] (see also [19, 38] for the generalization) that $\{a^H; b_1, \ldots, b_m\}$ is a tight framelet filter bank such that all the highpass filters $b_1, \ldots, b_m$ have only two taps and exhibit $\frac{1}{2}(3^d - 1)$ directions in dimension d. In particular, for $d = 1$, the tight framelet filter bank is just the standard Haar orthogonal wavelet filter bank $\mathrm{DHF}_1 := \{a^H; b\}$ with $a^H = \frac{1}{2}(\boldsymbol{\delta}_0 + \boldsymbol{\delta}_1)$ and $b = \frac{1}{2}(\boldsymbol{\delta}_0 - \boldsymbol{\delta}_1)$. For $d = 2$, the corresponding tight framelet filter bank reduces to the directional Haar tight framelet filter bank $\mathrm{DHF}_2 := \{a^H; b_1, \ldots, b_6\}$ in [21, (3.5)].

For $d = 3$, it is a 3D directional Haar tight framelet filter bank $\mathrm{DHF}_3^1 := \{a^H; b_1, \ldots, b_{28}\}$ with $a^H = \frac{1}{8}(\boldsymbol{\delta}_{(0,0,0)} + \boldsymbol{\delta}_{(0,0,1)} + \boldsymbol{\delta}_{(0,1,0)} + \boldsymbol{\delta}_{(0,1,1)} + \boldsymbol{\delta}_{(1,0,0)} + \boldsymbol{\delta}_{(1,0,1)} + \boldsymbol{\delta}_{(1,1,0)} + \boldsymbol{\delta}_{(1,1,1)})$ and the 28 filters $b_\iota = \frac{1}{8}(\boldsymbol{\delta}_{\gamma_1^\iota} - \boldsymbol{\delta}_{\gamma_2^\iota})$ for $\iota = 1, \ldots, 28$. Since we employ the UDFmT (undecimated discrete framelet transforms) for the W_{3D} in our model (1.5), only the partition of unity condition is needed ($\omega = 0$ in (2.1)) to guarantee the perfect reconstruction property. Hence, by considering filters with the same direction, the 28 high-pass filters in DHF_3^1 can be regrouped to 13 filters as a filter bank DHF_3^2 with filters a^H, b_x, b_y, b_z, $b_{xy}, b_{x,y}, b_{xz}, b_{x,z}, b_{yz}, b_{y,z}$, $b_{xyz}, b_{xy,z}, b_{x,yz}, b_{xz,y}$ in [23]. Furthermore, as demonstrated in [22], the output framelet coefficient sequences involving the z-filters, i.e., those b_z, b_{xz}, b_{xyz}, etc., are actually 'bad' features for our 3D signal reconstruction. They represent local contrast discrepancy between coil images which do not play a role in our restriction process. Hence, in [22], the filter bank DHF_3^2 is further simplified to the filter bank $\mathrm{DHF}_3^3 := \{a^H; b_x, b_y, b_{xy}, b_{x,y}, b_{\mathrm{aux}}\}$, where $b_x = \frac{1}{4}(\boldsymbol{\delta}_{(1,0,0)} - \boldsymbol{\delta}_{(0,0,0)})$, $b_y = \frac{1}{4}(\boldsymbol{\delta}_{(0,1,0)} - \boldsymbol{\delta}_{(0,0,0)})$, $b_{xy} = \frac{\sqrt{2}}{8}(\boldsymbol{\delta}_{(1,1,0)} - \boldsymbol{\delta}_{(0,0,0)})$, $b_{x,y} = \frac{\sqrt{2}}{8}(\boldsymbol{\delta}_{(1,0,0)} - \boldsymbol{\delta}_{(0,1,0)})$, and the filter b_{aux} is determined by $\widehat{b_{\mathrm{aux}}} := 1 - (|\widehat{a^H}|^2 + |\widehat{b_x}|^2 + |\widehat{b_y}|^2 + |\widehat{b_{x,y}}|^2 + |\widehat{b_{xy}}|^2)$.

The 3D directional Haar filter bank DHF_3^3 nicely fits into our SENSE pMRI regularization and reconstruction with the following properties: (a) the lowpass filter a^H produces an underlying image with harmonic pixel intensity for further process by the directional highpass filters; (b) the directional highpass filters $b_x, b_y, b_{xy}, b_{x,y}$ are properly chosen to capture the edge information for the sparse representation, which facilitates the successful recovery in the ℓ_1-based optimization models; (c) the auxiliary filter b_{aux} guarantees the perfect reconstruction of the 3D filter bank and the UDFmT, where in practice it does not participate in the shrinkage operation so that the procedure of UDFmTs is equivalent to the UDFmT using the tight framelet filter bank DHF_3^2. We refer to [22, 23] for the detailed construction of the DHF_3^3 and the implementation of the UDFmT based on the DHF_3^3.

3. Optimization models and the *SENSE3d*-algorithm. The problem (1.1) is highly ill-posed, because different pairs of u and s_ℓ can bring about the same g_ℓ. Under the priori knowledge about u and s_ℓ, our goal is to approximate the desired image u when s_ℓ are unknown and the acquired K-space signal g_ℓ are incomplete. To achieve this goal, we introduce a so-called *SENSE3d*-algorithm for finding an estimate of both u and s_ℓ. The basic steps for the *SENSE3d*-algorithm are outlined in Algorithm 3.1.

Algorithm 3.1 The *SENSE3d*-Algorithm

1: Given the observed K-space signal g_ℓ, sampling matrix P and an initial sensitivity matrices s_ℓ^0, $\ell = 1, 2, \ldots, L$.
2: **for** $k = 1, 2, \ldots$ **do**
3: Slice-step: Find an estimate of u from the observed K-space signals g_ℓ and the estimated sensitivity matrices s_ℓ;
4: Sensitivity-step: Update the sensitivity vectors s_ℓ, for $\ell = 1, 2, \ldots, L$, from the observed K-space signal g_ℓ and the estimated image u.
5: **end for**
6: Return u^∞ the estimate of the desired image u.

The *SENSE3d*-algorithm is an iterative way to find the estimate of u by decoupling the effects of u and the sensitivity maps s_ℓ. We remark that a model called JSENSE that alternatively estimates the slice image u and the sensitivity vectors s_ℓ was proposed in [44] but it is without considering any regularization technique and the convergence analysis. On the other hand, in the Slice-step of Algorithm 3.1 for our SENSE3d model, we integrate in the regularization with the novel 3D directional Haar filter bank DHF_3^3 that captures the sparsity of the coils image. In the Sensitivity-step of Algorithm 3.1, we propose a Tikhonov-type regularization that favors the smoothness of the sensitivity mapping s_ℓ, $\ell = 1, 2, \ldots, L$. For the regularized optimization problems in the Slice-step and Sensitivity-step, we develop efficient algorithms to solve them and provide convergence analysis to these algorithms.

3.1. Slice-step: Object estimation. We begin by introducing the basic notation. The pMRI acquisition model involves complex numbers. For a vector $u \in \mathbb{C}^n$, we use $\|u\|_2 := \sqrt{\sum_{j=1}^n |u[j]|^2}$, $\|u\|_1 := \sum_{j=1}^n |u[j]|$, and $\|u\|_\infty := \max_{1\leqslant j\leqslant n} |u[j]|$ to represent, respectively, the ℓ_2-, ℓ_1-, and ℓ_∞-norm of u, where $u[j]$ is the jth component of u. For a matrix $A \in \mathbb{C}^{m\times n}$, we define its norm as follows:

$$\|A\|_2 := \max\{\|Au\|_2 : u \in \mathbb{C}^n \text{ with } \|u\|_2 = 1\}.$$

Hereafter, $\mathrm{Re}(\cdot)$ and $\mathrm{Im}(\cdot)$ stand for the real and imaginary parts, respectively. For $u \in \mathbb{C}^n$, we have $u = \mathrm{Re}(u) + i\mathrm{Im}(u)$, where both $\mathrm{Re}(u)$ and $\mathrm{Im}(u)$ are in $\mathbb{R}^n$ and i is the imaginary unit satisfying $i^2 = -1$.

For the purpose of the exposition of optimization algorithms on $\mathbb{C}^n$, the inner product of two vectors u and v in $\mathbb{C}^n$ is defined as

$$\langle u, v\rangle := \mathrm{Re}(u^\top v), \tag{3.1}$$

where $u^\top$ is the conjugate transpose of u. With this inner product, the vector space $\mathbb{C}^n$ is actually viewed as the vector space $\mathbb{R}^{2n}$.

From the observed K-space signals g_ℓ and the estimated sensitivity maps s_ℓ, we propose to estimate u in (1.1) through an optimization model that is regularized by the prior knowledge of the coil images. Note that the ℓ-th coil image $s_\ell \odot u = \mathrm{diag}(s_\ell)u = S_\ell u$. From the identities $S_\ell u = F^{-1}FS_\ell u$ and $I_n = (I_n - P) + P$, in the noise-free situation we have

$$S_\ell u = F^{-1}((I_n - P)FS_\ell u + PFS_\ell u) = F^{-1}(I_n - P)FS_\ell u + F^{-1}g_\ell$$

for all $\ell = 1, 2, \ldots, L$. Putting all L coil images together, the above equations yield

$$c = Nu + (I_L \otimes F^{-1})g, \tag{3.2}$$

where $c = Su$ and $N = (I_L \otimes (F^{-1}(I_n - P)F))S$. Here, S is defined in (1.2) and $\otimes$ denotes the *Kronecker product*. Equation (3.2) says that the integration of the coil images c is composed of the missing information Nu and the available information $(I_L \otimes F^{-1})g$.

Denoting $W := W_{3D}$ the transformation matrix associated with the filter bank DHF_3^3 onto the coil images c, we have $Wc = W(Nu + (I_L \otimes F^{-1})g)$. Using this identity, (1.3), and (3.2), we propose to estimate image u through the following optimization problem

$$\min\left\{\frac{1}{2}\|Mu - g\|_2^2 + \|\Gamma W(Nu + (I_L \otimes F^{-1})g)\|_1 : u \in \mathbb{R}^n\right\}, \tag{3.3}$$

where Γ is a diagonal matrix with non-negative diagonal entries. In the objective function of (3.3), the term $\frac{1}{2}\|Mu - g\|_2^2$ measures the faithfulness of the recovered image to the given data while the term $\|\Gamma W(Nu + (I_L \otimes F^{-1})g)\|_1$ relates to the sparsity of the coil images $Nu + (I_L \otimes F^{-1})g$ under W. Note that the ideal image u is restricted in $\mathbb{R}^n$.

With the above preparation, we first present the PD3O (primal-dual three-operator) algorithm for solving (3.3) and the convergence analysis of the sequence generated by the algorithm. We postpone the discussion on the development and the convergence analysis of the algorithm in the Appendix 6.1 to avoid a lengthy digression.

This algorithm is written as follows: given the initial guess $(v^0, z^0) \in \mathbb{C}^n \times \mathbb{C}^d$ and the parameters γ, δ and Γ, iterate

$$\begin{cases} u^k &= \mathrm{Re}(v^k) \\ w^k &= (I - \gamma\delta AA^\top)z^k + \delta A(\bar{v}^k - \gamma M^\top(Mu^k - g)) \\ z^{k+1} &= (w^k + \delta b) - \mathrm{soft}(w^k + \delta b, \Gamma) \\ v^{k+1} &= u^k - \gamma M^\top(Mu^k - g) - \gamma A^\top z^{k+1}. \end{cases}$$

Here, $A = WN$, $b = W(I_L \otimes F^{-1})g$ and w^k is the auxiliary variable. Furthermore, soft is the well-known soft shrinkage operator, i.e., for $w \in \mathbb{C}^d$,

$$(\mathrm{soft}(w, \Gamma))[j] = \max\{|w[j]| - \Gamma[j,j], 0\}\frac{w[j]}{|w[j]|}$$

for $j = 1, 2, \ldots, d$. One iteration of the above scheme can be viewed as the operator $\mathrm{T}_{\mathrm{PD3O}}$ (see (6.3a)–(6.3c) in Appendix 6.1 for its definition) such that $(v^{k+1}, z^{k+1}) = \mathrm{T}_{\mathrm{PD3O}}(v^k, z^k)$.

The theorem for the convergence analysis of the PD3O algorithm for problem (3.3) is given as follows.

Theorem 3.1. *Let the pair $(v^\star, z^\star)$ be any fixed point of the $\mathrm{T}_{\mathrm{PD3O}}$ operator. Let κ be defined by*

$$\kappa = \max_j \sum_{\ell=1}^{L} |s_\ell[j]|^2 \tag{3.4}$$

and let $\{v^k, z^k\}_{k\geqslant 0}$ be the sequence generated by the PD3O algorithm (6.3a)–(6.3c) with

$$(v^{k+1}, z^{k+1}) = \mathrm{T}_{\mathrm{PD3O}}(v^k, z^k)$$

and the initial guess (v^0, z^0). Choose γ and δ such that $\gamma < 2/\kappa$ and $\gamma\delta < 1/\kappa$. Define $B := \frac{\gamma}{\delta}(I - \gamma\delta AA^\top)$ and $\|(v,z)\|_B := \sqrt{\|v\|^2 + \langle z, Bz\rangle}$. Then, the following statements hold.

(i) *The sequence $\{\|(v^k, z^k) - (v^\star, z^\star)\|_B\}_{k\geqslant 0}$ is monotonically nonincreasing.*

(ii) *The sequence $\{\|(v^{k+1}, z^{k+1}) - (v^k, z^k)\|_B\}_{k\geqslant 0}$ is monotonically nonincreasing. Moreover, we have $\|(v^{k+1}, z^{k+1}) - (v^k, z^k)\|_B = o\left(\frac{1}{k+1}\right)$.*

The detailed proof of the above theorem is given in Appendix 6.1. We next focus on the estimation of the sensitivity maps s_ℓ.

3.2. Sensitivity-step: Sensitivity maps estimation.

Once we have an approximation to the target image u, we can use it to update the sensitivity maps s_ℓ, $\ell = 1, 2, \ldots, L$. From the acquisition model (1.1) and the facts that $I_n = P + (I_n - P)$ and $g_\ell = PF(s_\ell \odot u)$ in the noise-free case, the approximation of the full K-space signal, denoted by $g_{est,\ell}$ and received by the ℓth coil, can be modeled as

$$g_{est,\ell} = g_\ell + (I_n - P)F(s_\ell \odot u). \tag{3.5}$$

That is, $g_{est,\ell}$ is composed of the observed partial K-space information g_ℓ and the estimated unobservable K-space data $(I - P)F(s_\ell \odot u)$. In the noise-free case, due to $s_\ell \odot u = u \odot s_\ell = \mathrm{diag}(u)s_\ell$, we indeed have

$$g_{est,\ell} = F(s_\ell \odot u) = (F\mathrm{diag}(u))s_\ell. \tag{3.6}$$

Define

$$g_{est} = \begin{bmatrix} g_{est,1} \\ \vdots \\ g_{est,L} \end{bmatrix}, Q = I_L \otimes (F\mathrm{diag}(u)), s = \begin{bmatrix} s_1 \\ \vdots \\ s_L \end{bmatrix}. \tag{3.7}$$

Here, $g_{est} \in \mathbb{C}^{Ln}$, $Q \in \mathbb{C}^{Ln\times Ln}$, and $s \in \mathbb{C}^{Ln}$. With these preparations, a compact representation of (3.6) is as follows:

$$g_{est} = Qs. \tag{3.8}$$

To estimate a faithful s from model (3.8), we should take both reliable K-space data information from g_{est} and prior knowledge on s into consideration. Regarding the prior knowledge on s, each sensitivity map s_ℓ is assumed to be smooth and the energy of the values coming from the same location of the sensitivity maps is identical and equals to one, that is, $\sum_{\ell=1}^{L} |s_\ell[j]|^2 = 1$, for all $j = 1, \ldots, n$, see [24]. Due to $u \odot s_\ell = (hs_\ell) \odot (u/h)$ holds for any nonzero constant h, the constraint on the sensitivity maps s_ℓ ensures the uniqueness of the underlying problem. Therefore, we define the domain

$$D := \{s : s \in \mathbb{C}^{Ln}, \sum_{\ell=1}^{L} |s[j + (\ell - 1)n]|^2 = 1 \text{ for } j = 1, \dots, n\}. \tag{3.9}$$

With these preparations, our proposed optimization problem for estimating s from model (3.8) has a form of

$$\min \left\{ \frac{1}{2} \|P_{sel}(Qs - g_{est})\|_2^2 + \frac{1}{2} \|\Gamma_s W s\|_2^2 : s \in D \right\}, \tag{3.10}$$

where P_{sel} is a sampling matrix and $W = W_{3D}$ is associated with the 3D directional Haar framelet transform used in the Slice-step. Here Γ_s is a diagonal matrix whose diagonal entries corresponding to the framelet coefficients from lowpass filter of the framelet system are zero and the others have the same value. The use of P_{sel} here is twofold. First, the *K*-space data is usually fully sampled near its center, i.e., the ACS lines, and thus gives more accurate estimation of g_{est} near the center. The sampling matrix P_{sel} is hence defined to sample coefficients near the center of *K*-space only. Second, the smooth assumption on each s_ℓ implies that the frequency response of s_ℓ is concentrated around the center of the *K*-space (a low-passed signal). Therefore, there is no need to use the full *K*-space data. Moreover, P_{sel} reduces the computation cost significantly. In our experiments, P_{sel} is indeed the sampling matrix corresponding to the ACS line.

Since the objective function of the optimization problem (3.10) is Lispchitz continuous, problem (3.10) can be solved through the forward-backward algorithm (see, for example, [1]). It reads as, for any initial guess s^0, iterate

$$s^{k+1} = \mathrm{proj}_D(s^k - \tau_k(Q^\top P_{sel}(Qs^k - g_{est}) + W^\top \Gamma^2 W s^k)), \tag{3.11}$$

where $\tau_k > 0$. Here, if $t = \mathrm{proj}_D(s)$ for $s \in \mathbb{C}^{Ln}$, then for each $j = 1, 2, \dots, n$, let $\tilde{t} = [t[j], t[j + n], \dots, t[j + (L - 1)n]]$ and $\tilde{s} = [s[k], s[k + n], \dots, s[k + (L - 1)n]]$, we have

$$\tilde{t} = \begin{cases} \frac{\tilde{s}}{\|\tilde{s}\|_2}, & \text{if } \|\tilde{s}\|_2 \neq 0; \\ \text{any unit-vector in } \mathbb{C}^L, & \text{otherwise.} \end{cases}$$

The convergence analysis of the iterative scheme (3.11) is given in the following theorem.

Theorem 3.2. *Given an* $\epsilon \in \left(0, \frac{1}{2(\|u\|_\infty^2 + \|\mathrm{diag}(\Gamma)\|_\infty^2)}\right)$ *and a sequence of stepsize* τ_k *such that* $\epsilon < \tau_k < \frac{1}{\|u\|_\infty^2 + \|\mathrm{diag}(\Gamma)\|_\infty^2} - \epsilon$, *we consider the sequence* $\{s^k\}_{k \geqslant 0}$ *generated by* (3.11). *Then the sequence converges to a point* $s^\star$ *in* D *such that*

$$Q^\top P_{sel}(Qs^\star - g_{est}) + Q^\top \Gamma^2 Q s^\star + \nu \mathrm{diag}(I_L \otimes \nu) s^\star = 0$$

for some vector $\nu \in \mathbb{R}^n$ *with positive* $\nu_i \geqslant 0$, $i = 1, 2, \dots, n$.

The proof of the above theorem is given in Appendix 6.2.

4. Experiments.

In this section, we provide numerical experiments to demonstrate the performance of our *SENSE3d* model. We begin by reviewing some related work on SENSE and GRAPPA. We then provide numerical experiments for the comparisons of our model with some traditional methods as well as some deep learning methods.

4.1. Related work.

For the SENSE method, total variation (TV) is one of the regularization techniques that has an ability to recover the edge details in the target image for the pMRI problem [43]. It is well known that TV does not distinguish between jumps and smooth transitions, and tends to give piecewise constant images with staircase artifacts. Total generalized variation (TGV) with high-order differential operator can remove the staircase artifacts caused by TV, and the TGV of second-order is applied to parallel imaging in [17]. Wavelet transforms are adopted to detect artifacts appeared in the basic SENSE reconstruction and reduce the artifacts by emphasizing the sparse representation of the underlying image [4]. However, the reconstructed image will suffer from ringing artifacts when the wavelet coefficients are modified in an incorrect way. The 2D directional Haar framelet (DHF) based regularization technique assimilating the advantages of both total variation and wavelet regularization, called FADHFA, was proposed for SENSE to preserve details of slice and remove noise in [21]. To adaptively represent the image with sparse canonical coefficients by tight frame, a data-driven tight frame based off-the-grid regularization model was proposed for the compressive sensing MRI reconstruction in [3]. The non-convex and non-smooth Euler's elastica functional was proposed to regularize SENSE reconstruction in [42]. These 2D regularization techniques only focus on each coil image independently, and the redundant information among multi-coil images of pMRI are not considered in the SENSE reconstructions.

The generalized autocalibrating partially parallel acquisitions (GRAPPA) in [9] is a *K*-space method and interpolates the missing data in the *K*-space for each coil from the multi-coil neighbouring *K*-space samples. The GRAPPA method can reconstruct almost the same quality of images as those from the SENSE method [2], but it requires the ACS data, near the center of *K*-space, to estimate the interpolation weights or coil sensitivities. In [37], sparsity-promoting calibration was proposed to regularize the GRAPPA-based interpolation weights for reconstructing high quality MRI images. By exploiting the nonlinear relationship between ACS and missing data, a kernel-based approach was suggested to interpolate the missing data in the *K*-space [25]. Iterative self-consistent parallel imaging reconstruction (SPIRiT) extends the GRAPPA's interpolation weights on sampled and unsampled data and fills missing *K*-space as an inverse problem [24]. ESPIRiT is a "soft" SENSE reconstruction using the eigenvectors of a calibration matrix constructed by the SPIRiT model as sensitivity maps, and is called ℓ_1-ESPIRiT by regularizing the wavelet coefficients of the target images with ℓ_1 norm [33]. Joint sparsity of the wavelet coefficients of each coil image at same position is applied to SPIRiT model (ℓ_1-SPIRiT) [27] and SENSE model (JSCSSENSE) [5] to further improve the quality of the reconstruction results. Since ESPIRiT does not consider the phase of image, an algorithm called VCC-ESPIRiT [34] incorporating the virtual conjugate coils was proposed to estimate the sensitivity maps that include the absolute phase of the image. A 3D directional Haar tight framelet (3DHF) was proposed to regularize the related features between coil images reconstructed by SPIRiT model for reducing the aliasing artifacts caused by the downsampling operation [23].

The filling of *K*-space dada was formulated as the low-rank matrix completion problem in [14]. The low-rank matrix modeling of local *K*-space neighborhoods (LORAKS) [10], and simultaneous autocalibration and *K*-space estimation (SAKE) [31] use local neighborhoods of multi-coil *K*-space data to construct low-rank matrices for regularizing parallel imaging reconstruction. Under smooth phase assumptions, the LORAKS method also imposes phase constraints on low-rank matrices. When an image is with the finite rate of innovation, then its *K*-space data has a property with low-ranked weighted Hankel structured matrix, leading to an annihilating filter-based low rank Hankel matrix approach (ALOHA) [15]. Jointing sparsity of the patches from multi-coil images using sparse dictionary was proposed to regularize the reconstruction coil MR images by considering the cross-channel relationships in [36].

Deep learning methods based on many neural network architectures can discover the internal relationship of large-scale data through training and learning, and make multi-level abstract representation of data [40, 41]. A deep convolutional neural network was proposed to learn regularization part of the optimization model for inverse problem and applied to the pMRI problem in [16]. U-Net is a commonly used neural network model in medical image processing [30], and has been successfully applied to MRI reconstruction [32,45]. An end-to-end variation network (VarNet) [32] is a more powerful model built upon the fastMRI-UNet model [45]. The VarNet model utilizes a sensitivity map estimation module, a refinement module, and a data consistency module to estimate missing *K*-space data and reconstruct MRI images. It achieves good results on the fastMRI dataset and served as the baseline model for the 2020 fastMRI challenge [26].

Deep learning methods for pMRI reconstruction require large number of multi-coil *K*-space data and accurate information about the MR machine acquisitions, however, the parameters of the imaging setting of MRI machine (for example, field of view, slice thicknesses, and others) maybe different for different cases. For example, a person's heartbeat, slight body jitter and other factors in the process of scanning can form gradient information similar to adversarial attack, which affects the accuracy of prediction and results in blurred anatomical structure details and artifacts in reconstructed MRI images using deep learning methods [8]. Hence, in this paper, we focus on approaches without the needs of large scale data but simply with the few given multi-coil data in the pMRI reconstruction. Nevertheless, we provide comparisons of our methods with the deep learning methods as well.

4.2. Parameter settings. The parameter setting of our *SENSE3d*-algorithm is as follow. In the Slice-step, the parameters $\gamma = 1.99$, $\delta = 0.5$, and for a more precise choice of Γ, the thresholding parameter, we refer to [22, Section 4.2]; In the Sensitivity-step, all nonzero diagonal entries of the diagonal matrix Γ are identical, say each s-th diagonal entry $\lambda_s = 0.05$ for all experiments. After this parameter is determined, we choose $\tau_k = \frac{0.99}{2(\|u\|_\infty^2 + \lambda_s^2)}$ and 25 iterations for Sensitivity-step. We terminate our method when $\|u^{k+1} - u^k\|_2^2 / \|u^k\|_2^2 < 10^{-6}$ or when the number of iterations exceeds 40. Here u^k is the kth iteration produced by the underlying algorithm. Our *SENSE3d*-algorithm only updates the sensitivity maps at $k = 8$, 16 and 24 by the Sensitivity-step, and then fixes them after $k = 24$ to guarantee convergence in Slice-step. The two-level decomposition of DHF_3^3 is adopted in all experiments.

Several state-of-the-art methods reviewed above, including the fast adaptive DHF algorithm FADHFA [21], the ℓ_1-ESPIRiT method [33], and ALOHA [15], are adopted to further compare with our *SENSE3d* model in numerical experiments. The source code of the ℓ_1-ESPIRiT method was downloaded from the website of Michael Lustig[1], and its default settings are used except for kernel size with 5×5, maximal iteration 50 and regularization parameter λ set by hand for its best performance.

[1]The code is available at: http://people.eecs.berkeley.edu/~mlustig/Software.html

The source code of ALOHA method is available at this website of BISPL[2], and its default settings are used except for the follows: pyramidal decomposition with decreasing LMaFit tolerances, annihilating filters, and smoothed regularization parameter named as $sroi$.

To evaluate the performance of the algorithms for removing artifacts and preserving details, we use the HaarPSI index to calculate the similarity between the reference image and the reconstructed image [29][3]. The HaarPSI index ranges from 0 to 1, and higher value means that the algorithm is better to reconstruct details of slice and remove artifacts.

The experiments will be carried out on the real phantom and in-vivo data to test different pMRI reconstruction algorithms. The phantom MR images are acquired on a 3T MRI System (Tim Trio, Siemens, Erlangen, Germany). A turbo spin-echo sequence was used to acquire T_2-weighted images. The detailed imaging parameters are as follows: field of view (FOV) = 256×256 mm^2, image marix size = 512×512, slice thicknesses (ST) = 3 mm, flip angle = 180 degree, repetition time (TR) = 4000 ms, echo time (TE) = 71 ms, echo train length (ETL) = 11 and number of excitation (NEX) = 1.

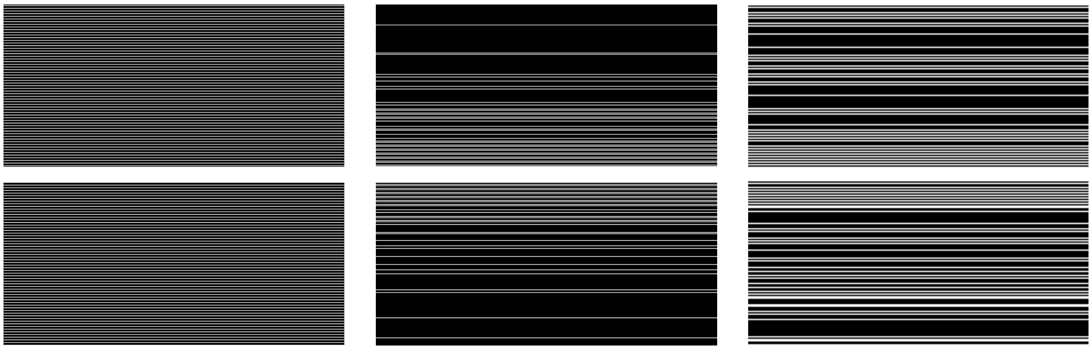

(a) 512-29%-24 (b) 512-18%-25 (c) 256-34%-11

Figure 3. *Sampling modes for the K-space. (a)* 29% *data by the uniform sampling model of* 512×512 *(one line taken from every four lines) with 24 ACS lines (the middle white area); (b)* 18% *data by the random sampling model of* 512×512 *with 25 ACS lines; (c)* 34% *data by the random sampling model of* 256×256 *with 11 ACS lines.*

4.3. Comparisons with other methods: MRI phantoms. In this subsection, three pMRI reconstruction methods FADHFA [21], ℓ_1-ESPIRiT [33] and ALOHA [15] are compared with our proposed *SENSE3d* model on the two slices of the MRI phantoms.

We first use four MRI phantom images under the 512×512 (512-29%-24) sampling model as shown in Fig. 3(a). That is, the uniform sampling model of 512×512 with one line taken from every four lines and with 24 ACS lines. In Fig. 4, the part (a) is the SoS image reconstructed from the full *K*-space data, while the part (b) is the SoS image with blurring and aliasing artifacts by four coil images from the downsampled *K*-space data by the uniform sampling mode in Fig. 3(a). The regularization parameter λ is to be 0.035 and 0.001 for ℓ_1-ESPIRiT and our *SENSE3d* model, respectively. The settings for ALOHA are four levels of pyramidal decomposition with decreasing LMaFit tolerances $(0.3, 0.03, 0.003, 0.0003)$, annihilating filters with size of 11×11 , and $sroi = 10$.

The four pMRI reconstruction algorithms can retrieve most of the information from the parts of

[2]The code is available at: https://bispl.weebly.com/aloha-for-mr-recon.html
[3]The code is available at: http://www.math.uni-bremen.de/cda/HaarPSI/

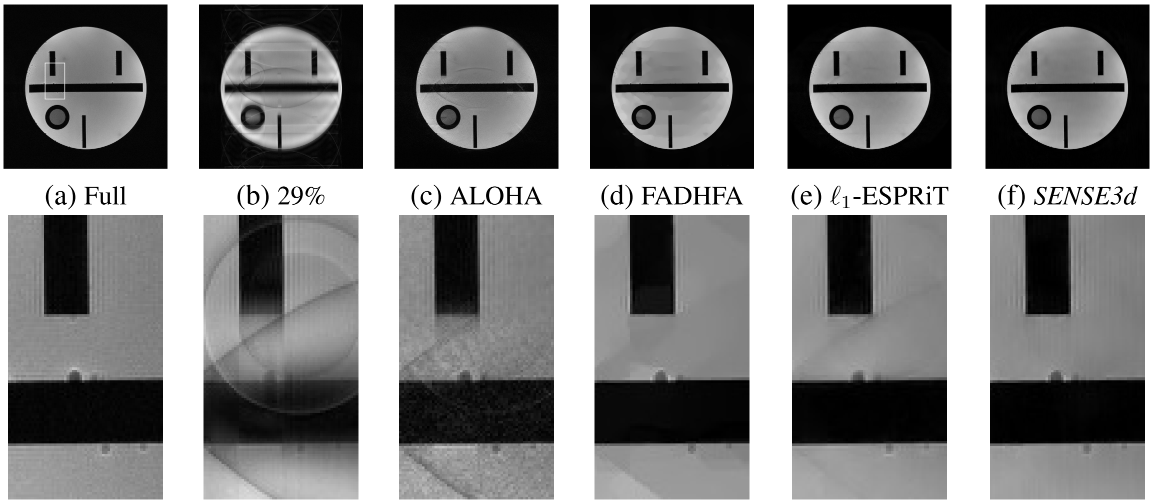

(a) Full (b) 29% (c) ALOHA (d) FADHFA (e) ℓ_1-ESPRiT (f) *SENSE3d*

(a') Full (b') 29% (c') ALOHA (d') FADHFA (e') ℓ_1-ESPRiT (f') *SENSE3d*

Figure 4. *MRI Phantoms of Slice 1 with size 512-by-512. (a) Reference SoS image by four full K-space data with zoom-in area. (b) SoS image by four coil images by 29% K-space data on uniform sampling mode in Figure 3(a). (c) ALOHA. (d) FADHFA. (e) ℓ_1-ESPRiT. (f) Our proposed 3D-US model. (a')–(f') are the zoom-in parts of (a)–(f), respectively.*

the K-space data, but the images in Figs. 4(c), (d) and (e) by ALOHA, FADHFA and ℓ_1-ESPIRiT respectively, have some obvious aliasing artifacts, which are removed by our *SENSE3d* model and do not appear in Fig. 4(f). That is to say, the correlated features by 3D tight framelet can be utilized to regularize the reconstruction image. We provide the zoom-in parts of the reconstructed images in Figs. 4(a')–(f') for distinguishing their difference. One can see that the 'circle' and 'line' false aliasing artifacts in (b') are mostly reduced by the regularized algorithms, but false 'circle' structures on the black region and and noisy artifacts still appear in the zoom-in image (c') by low-rank regularization, while the 'line' artifact exists at the left-down corner of the zoom-in image (d') by 2D-U model and at the middle of the zoom-in image (e') by ℓ_1-ESPIRiT using 2D wavelet regularization without considering the correlated features of coil images. The Fig. 4(f') by our *SENSE3d* model does not have these aliasing artifacts and it removes noise and preserves details of the edges more closer to the reference image (a') with full K-space data. The HaarPSI indexes in Table 1 of these four zoom-in images by ALOHA, FADHFA , ℓ_1-ESPIRiT, and *SENSE3d* are 0.68, 0.81, 0.84 and 0.90, respectively. Our *SENSE3d* algorithm can get the highest index, which means that our SENSE3d model can efficiently remove artifacts and preserve details.

We next use four MRI phantom images under the 512×512 (512-18%-25) sampling model as shown in Fig. 3(b). That is, we use 18% sampling rate and 25 ACS lines to collect K-space data for this phantom slice. The parameter settings for ALOHA are four levels of pyramidal decomposition with decreasing LMaFit tolerances (0.3, 0.03, 0.003, 0.0003), 9×9 annihilating filers, and $sroi = 8$. The reconstructed results by ALOHA, FADHFA, ℓ_1-ESPIRiT with regularization parameter $\lambda = 0.025$ and the proposed *SENSE3d* model with parameter $\lambda = 0.0002$ are shown in Figs. 5(c), (d), (e) and (f), respectively.

Due to the downsampling operation on the K-space, the SoS image in Fig. 5(b) from 18% K-space data is blurry and has lots of aliasing artifacts. The ALOHA, FADHFA, ℓ_1-ESPIRiT and proposed

Table 1

The HaarPSI indexes of the zoom-in parts of reconstructed images by ALOHA, FADHFA , ℓ_1-ESPIRiT, and SENSE3d *in Algorithm 3.1 for removing artifacts and preserving details.*

Algorithm	ALOHA	FADHFA	ℓ_1-ESPIRiT	*SENSE3d*
	Zoom-in parts in Figures			
Fig. 4	0.68	0.81	0.84	**0.90**
Fig. 5	0.73	0.85	0.86	**0.92**
Fig. 7				
First row	0.89	0.93	0.95	**0.96**
Second row	0.87	0.90	0.93	**0.96**

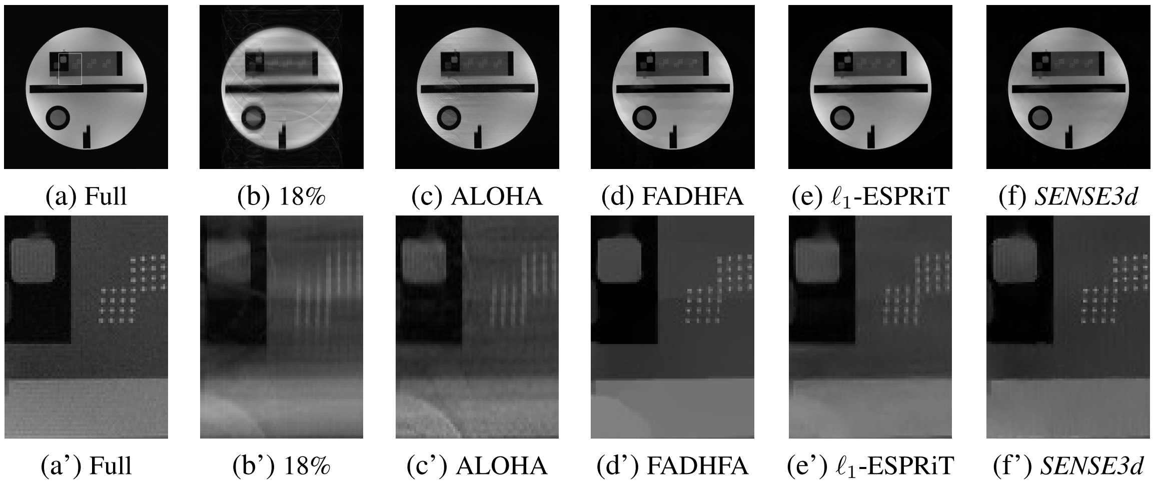

Figure 5. *MRI Phantoms of Slice 2 with size 512-by-512. (a) Reference SoS image by four full K-space data, (b) SoS image by 18% K-space data with sampling model in Figure 3(b). (c) ALOHA. (d) FADHFA. (e) ℓ_1-ESPRiT. (f) Our proposed* SENSE3d *model. (a')–(f') are the Zoom-in parts of (a)–(f), respectively.*

SENSE3d model can reconstruct most of details of the target slice and reduce aliasing with respect to reference image by full *K*-space data in Figs. 5(c)–(f). However, the Fig. 5(c) by the ALOHA method has obvious aliasing artifacts and false structures, which is not suitable for doctor's diagnosis. We present the zoom-in parts of the reconstruction images into Figs. 5(a')–(f') to further compare these methods. It is obvious to see that our *SENSE3d* model can efficiently remove aliasing artifacts and keep the structures of the imaging slice. The ALOHA method is not efficient to preserve the shape of the bright 'points' and separate boundary between the upper and lower regions, and aliasing artifacts in the zoom-in images in Fig. 5(c'); The ℓ_1-ESPIRiT is better than ALOHA to retrieve the bright 'points' and reduce aliasing artifacts, but it is worse than the FADHFA and our *SENSE3d* model to preserve the boundary edges; The FADHFA is almost the same as the *SENSE3d* to preserve structure details of the slice, but the Fig. 5(d') by FADHFA has 'arc' artifacts at left-down of the zoom-in image and false 'gray' edges covering the regions of bright 'points'. The Fig. 5(e') by ℓ_1-ESPIRiT also has the aliasing artifact problem as that in Fig. 5(d') by FADHFA, but it is not efficient to preserve sharp edges and blurs these region. All the above issues in Figs. 5(c')–(e') do not appear in Fig. 5(f') by our *SENSE3d* model. The HaarPSI indexes in Table 1 of these four zoom-in images by ALOHA, FADHFA

, ℓ_1-ESPIRiT, and *SENSE3d* are 0.73, 0.85, 0.86 and 0.92, respectively. It shows that our *SENSE3d* model gives the best performance for reconstructing the slice image.

The 3D tight framelet regularization is essentially different from the 2D tight framelet regularization when extracting the features of the correlated coil images for pMRI reconstruction. Our *SENSE3d* model not only has merit of 2D tight framelet-based FADHFA to preserve details but also utilizes correlated features to remove aliasing artifacts caused by downsampling operation in *K*-space. This case again shows our *SENSE3d* pMRI reconstruction algorithm can reconstruct most details of the slice and remove aliasing artifacts when the accelerated sampling rate is high.

4.4. Comparisons with other methods: In-vivo data. In this subsection we test our *SENSE3d* model on MRI data that are obtained by head examination from a healthy volunteer. The detailed imaging was done on a 3T MRI system. Transverse T_2-weighted images were acquired with a turbo spin-echo sequence. The detail imaging parameters are as follows: field of view = 256 $\times$ 256 mm^2, image matrix size = 256 $\times$ 256, slice thicknesses = 3 mm, flip angle = 150 degree, repetition time = 5920 ms, echo time = 101 ms, echo train length = 11 and number of excitation = 1.

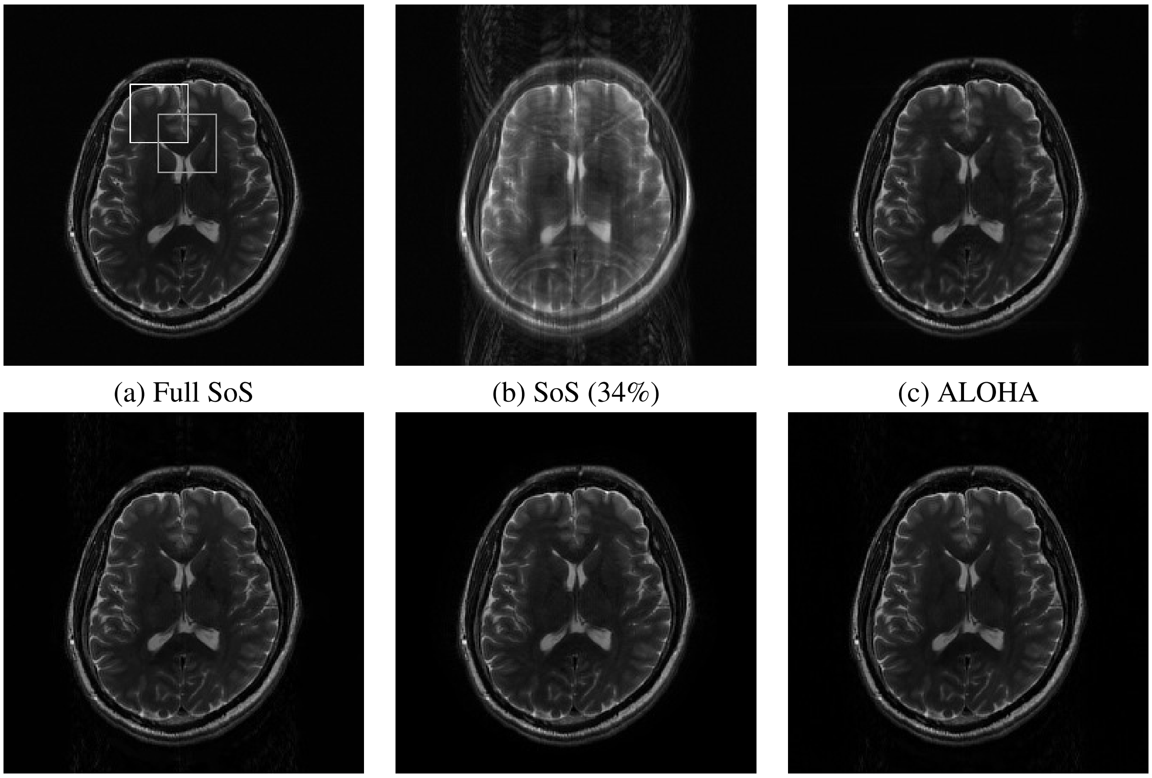

(a) Full SoS (b) SoS (34%) (c) ALOHA

(d) FADHFA (e) ℓ_1-ESPRiT (f) SENSE3d

Figure 6. *In-vivo data with sampling model* 256 $\times$ 256 *(256-34%-11) as shown in Fig. 3(c) with two to-be zoom-in square areas. (a) Reference SoS image of 32 coil images by full K-space data with two zoom-in regions. (b) SoS image by 34% K-space data. (c) ALOHA. (d) FADHFA. (e) ℓ_1-ESPRiT. (f) Our* SENSE3d *model.*

The magnetic resonance signal of each slice is received by 32 channels, and the reference image of one slice in Fig. 6(a) is a SoS image of 32 coil images by full of the *K*-space data. In phase direction,

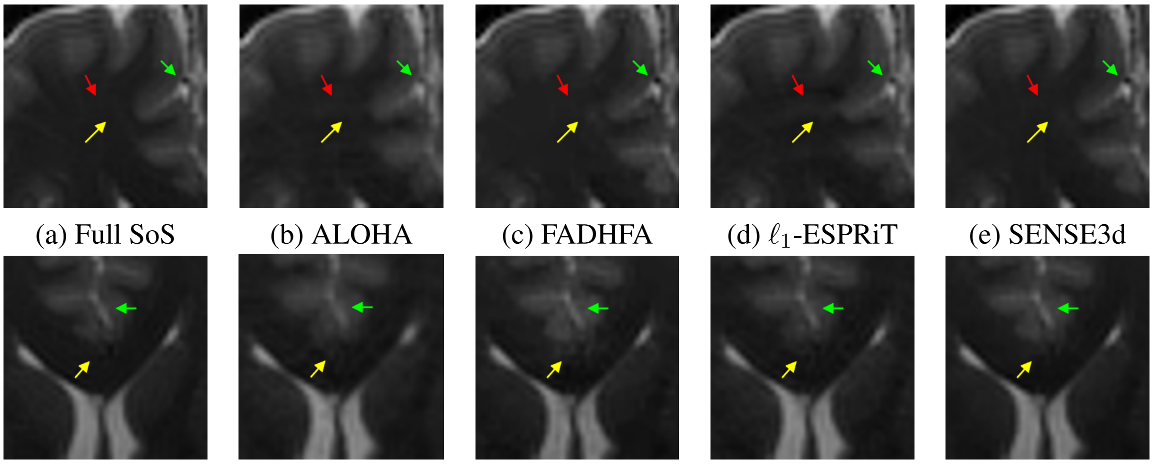

(a) Full SoS (b) ALOHA (c) FADHFA (d) ℓ_1-ESPRiT (e) SENSE3d

(f) Full SoS (g) ALOHA (h) FADHFA (i) ℓ_1-ESPRiT (j) SENSE3d

Figure 7. *Two zoom-in parts of Fig. 6. (a)(f) Reference SoS image. (b)(g) ALOHA. (c)(h) FADHFA. (d)(i) ℓ_1-ESPRiT. (e)(j) Our* SENSE3d *model.*

about 34% K-space data are collected using the pseudo-random sampling mode with 11 ACS lines in Fig. 3(c). The resulting SoS image of the collected 34% K-space data in Fig. 6(b) is noisy and the brain structures are blurry. Furthermore, faint semicircle-like aliasing artifacts can be seen in the upper and lower portions of the image due to the accelerating K-space sampling mode.

The reconstructions by the ALOHA, FADHFA, ℓ_1-ESPIRiT and our *SENSE3d* model are shown in Figs. 6(c), (d), (e) and (f), respectively. Their parameter settings are as follows: four levels of pyramidal decomposition with decreasing LMaFit tolerances (10^{-1}, 10^{-2}, 10^{-3}, 10^{-4}), 9×9 annihilating filers, and regularization parameter $sroi = 1.1$ for ALOHA; ℓ_1-ESPIRiT with $\lambda = 0.003$ and our 3D *SENSE3d*-Algorithm with $\lambda = 0.00001$. Clearly, the quality of the images in Figs. 6(c), (d), (e) and (f) are much better than the one in Fig. 6(b) in terms of the structures of the slice, the levels of noise and the aliasing artifacts.

To discriminate the difference of reconstructed images, we zoom-in two square regions as in Fig. 6(a) to compare the quality of the reconstructions by ALOHA, FADHFA, ℓ_1-ESPIRiT and our *SENSE3d* model. The first region at the left side of frontal lobe is zoomed-in and provided in Figs. 7(a)–(e). According to HaarPSI indexes in Table 1, the Figs. 7(b)–(e) by ALOHA, FADHFA , ℓ_1-ESPIRiT, and *SENSE3d* are 0.89, 0.93, 0.95 and 0.96, respectively. Our *SENSE3d* algorithm is the best to reconstruct slice details from in-vivo data.

We label three positions by red, green and yellow arrows to compare their differences by different algorithms. The artery pointed by green arrow in Fig. 7(b) by ALOHA is not clear and blurred, but structures of artery in Figs. 7(c), (d), and (e) respectively by FADHFA, ℓ_1-ESPIRiT and *SENSE3d* are more obvious than that by ALOHA. The FADHFA and *SENSE3d* models are better than the ℓ_1-ESPIRiT method, which reconstruct the structures of artery almost same as reference one in Fig. 7(a). At the region of white matter between red arrow and yellow arrow, there are aliasing artifacts in Fig. 7(d) by ℓ_1-ESPIRiT, extending from the frontal lobe into white matter; the boundary between the frontal lobe and white matter is blurry in Fig. 7(b) by ALOHA; there are 'white artifact' (yellow arrow pointing) in Fig. 7(b) by FADHFA; but Fig. 7(e) by our *SENSE3d* model doesn't have these aliasing problems and provides obvious boundary between tissues, and is very close to reference image in Fig. 7(a).

We zoom-in another part of slice at the anterior border of the corpus callosum region, and present zoom-in images in Figs. 7(f)–(j). The lobus (green arrow pointing) in Figs. 7(h), (i) and (j), respectively reconstructed by FADHFA, ℓ_1-ESPIRiT and our *SENSE3d*, still have better tissue structure than that in Fig. 7(g) by ALOHA. The low-rank regularized method ALOHA doesn't preserve details in the tissue. The yellow arrow pointing regions in Figs. 7(g), (h) and (i), respectively reconstructed by ALOHA, FADHFA, ℓ_1-ESPIRiT have aliasing artifacts at the anterior border of corpus callosum, which are false structures and do not appear in the reference image in Fig. 7(f). However, in Fig. 7(j), the aliasing artifacts is removed by our *SENSE3d* model and the geometry structures of the border is retrieved almost the same as the reference one. The HaarPSI indexes in Table 1, the Figs. 7(f)–(i) by ALOHA, FADHFA, ℓ_1-ESPIRiT, and *SENSE3d* are 0.87, 0.90, 0.93 and 0.96, respectively. The highest HaarPSI index of our *SENSE3d* algorithm is consistent with our visual observation. The ALOHA, FADHFA and ℓ_1-ESPIRiT methods are not very efficient to remove these artifact appeared in Fig. 6(b), but our *SENSE3d* model can be efficient to remove these aliasing artifacts and its reconstructed structures of tissues is close to reference image in Fig. 6(a). That is to say, 3D tight framelet-based *SENSE3d*-algorithm has a greater capacity of preserving edges and reducing most of the aliasing artifacts caused by downsamping operation in K-space than the 2D tight framelet-based, 2D wavelet-based and low-rank based regularization algorithms.

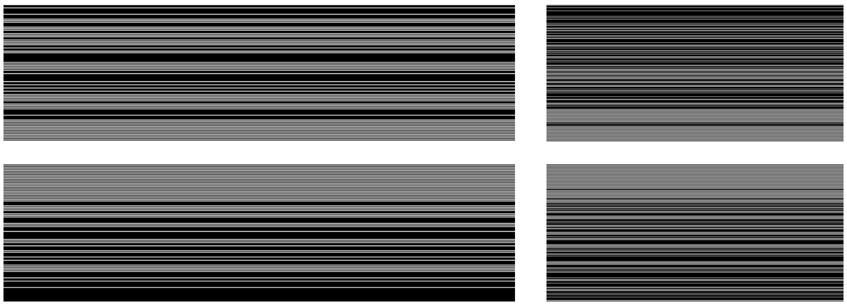

(a) 372-35%-30 (b) 770-35%-59

Figure 8. *Sampling modes for the K-space. (a)* 35% *data by the uniform sampling model of* 372×640 *with 30 ACS lines ; (b)* 35% *data by the random sampling model of* 770×768 *with 59 ACS lines.*

4.5. Comparisons with deep learning methods: Knee data. In this section, we compare our *SENSE3d* model with deep learning model VarNet [32][4] that is built upon the fastMRI-UNet model [45] with fastMRI dataset. [5]

A set of knee with full K-space data from the fastMRI dataset is used for this section. This knee dataset is acquired using a clinical 1.5T system with a 2D turbo spin-echo sequence and a conventional Cartesian 2D TSE protocol. The detailed imaging parameters are as follows: field of view = $280.00 \times 162.82 \times 4.50$ mm^3, image marix size = 640×372, slice thicknesses = 4.5 mm, flip angle = 140

[4] The code is available at: https://github.com/facebookresearch/fastMRI/tree/main/fastmri_examples/varnet

[5] The dataset is available at: http://fastmri.med.nyu.edu/ and served as the baseline model for the 2020 fastMRI challenge [26].

degree, repetition time = 2800 ms, echo time = 32 ms and echo train length = 4. The VarNet crops the reconstructed images from the network outputs with size 640×372 to be image blocks with size 320×320 centered on the original ones. We follow the settings of the VarNet model. The fully sampled images and reconstructed images by *SENSE3d* are also taken out from the same region for comparisons. Note that this knee dataset serves as a *validation set* for the VarNet model in training process. Hence, it is no doubt that the trained model VarNet gives superior performance on such data than the fastMRI-UNet model.

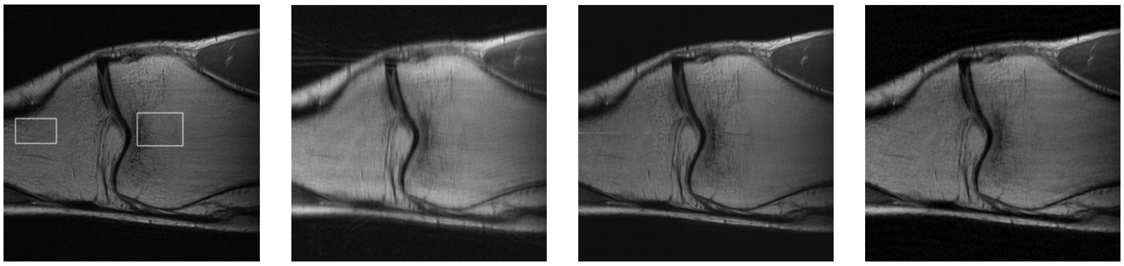

(a) Full SoS (b) SoS (35%) (c) VarNet (d) *SENSE3d*

Figure 9. *FastMRI data with sampling model 372-35%-30 as shown in Fig. 8(a) with two to-be zoom-in rectangle areas. (a) Reference SoS image of 15 coil images by full K-space data with two zoom-in regions. (b) SoS image by 35% K-space data. (c) VarNet. (d) Our* SENSE3d *model.*

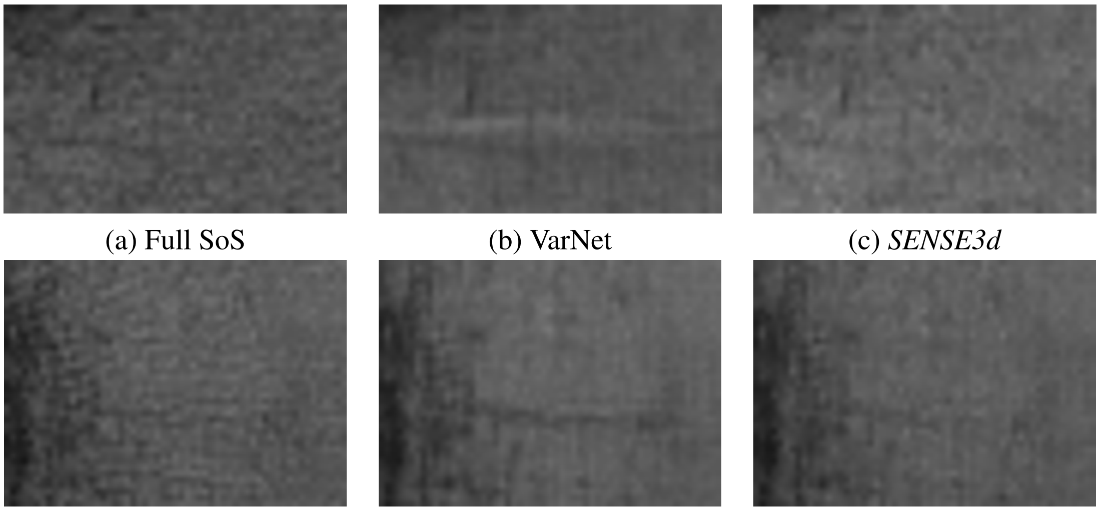

(a) Full SoS (b) VarNet (c) *SENSE3d*

(d) Full SoS (e) VarNet (f) *SENSE3d*

Figure 10. *Two zoom-in parts of Fig. 9. (a)(d) Reference SoS image. (b)(e) VarNet. (c)(f) Our* SENSE3d *model.*

The reference image in Fig. 9(a) is a SoS image by 15 coil images with full K-space data. In phase direction, about 35% K-space data are collected using the pseudo-random sampling mode with 30 ACS lines in Fig. 8(a). The resulting SoS image of the collected 35% K-space data in Fig. 9(b) is noisy and the knee structures are blurry. Furthermore, numerous faint elongated aliasing artifacts can be seen across the entire image due to the accelerating K-space sampling mode. The reconstructions by the

VarNet and our *SENSE3d* model are shown in Figs. 9(c) and (d), respectively. The parameter setting of our 3D *SENSE3d*-algorithm is $\lambda = 0.0005$, which remains the same throughout the subsequent experiments. Clearly, the quality of the images in Figs. 9(c) and (d) are much better than the one in Fig. 9(b) in terms of the structures of the slice, the levels of noise and the aliasing artifacts. To compare the difference between these two reconstructed images, we zoom-in parts of the femur and tibia regions and show them in Fig. 10. It is obvious that the zoom-in images by the VarNet are smoother than the original ones (lost of details) and have some aliasing artifacts, tibia image with 'white line' and femur image with 'black line'. But our SENSE3d algorithm can suppress these artifacts and its reconstructed images are with closer structures to the reference one. We provide their HaarPSI index for further comparisons. The HaarPSI index provided in Table 2 for tibia and femur images in Figs. 10(c) and (f) by our *SENSE3d* are 0.891 and 0.894, respectively. But the HaarPSI index by the VarNet in Figs. 10(b) and (e) are 0.866 and 0.879, respectively. Our *SENSE3d* gets higher HaarPSI index than that by the VarNet.

Table 2

The HaarPSI indexes of the zoom-in parts of reconstructed images by VarNet, fastMRI-UNet, and SENSE3d *in Algorithm 3.1 for removing artifacts and preserving details.*

Algorithm	Fig. 10		Algorithm	Fig. 12	
	First row	Second row		First row	Second row
VarNet	0.866	0.879	fastMRI-UNet	0.906	0.836
SENSE3d	**0.891**	**0.894**	*SENSE3d*	**0.970**	**0.961**

Another knee dataset is different from the data used in FastMRI, which is provided at this MRI data website [6]. This knee dataset is acquired using a clinical 2.89T system with a turbo spin-echo sequence. The detail imaging parameters are as follows: field of view = $280 \times 280.7 \times 4.5$ mm^3, image marix size = 768×770, slice thicknesses = 4.5 mm, flip angle = 150 degree, repetition time = 2800 ms, echo time = 22 ms.

We attempt to use the VarNet to reconstruct the MRI image on this new knee data. However, the VarNet cannot produce correct result on this new knee data. The main reason is due to the inaccurate sensitivity maps estimated by the VarNet besides the common generalization limitation of the network model such as inconsistent image from the fastMRI dataset, different machines data acquisition settings, and so on. We hence use another model, the fastMRI-UNet [45], that has less restrictions, to reconstruct the result and compare it with our model. Unlike the VarNet, the fastMRI-UNet directly takes K-space data as input and produces reconstructed MRI images, without the need for a sensitivity map estimation model. The source code of fastMRI-UNet is available at the GitHub website[7].

We use the sampling mode with 59 ACS lines in Fig. 8(b) to collect 35% K-space for the fastMRI-UNet and our SENSE3d to reconstruct the target image. The reconstructions by the fastMRI-UNet and our SENSE3d model are shown in Fig. 11(c) and (d) respectively. The SoS image in Fig. 11(b) by the collected 35% K-space data is blurry, but reconstructed images by the fastMRI-UNet and our SENSE3d model are clear with more structure details. To compare the difference between Fig. 11(c) and (d), we zoom-in parts of the popliteus and Soleus muscle regions and show them in Figure 10. The reconstructed images by our SENSE3d model are with clear organizational details than the images by

[6]http://www.mridata.org

[7]The code is available at: https://github.com/facebookresearch/fastMRI/tree/main/fastmri_examples/unet

the fastMRI-UNet. The popliteus part by our model is almost close to reference one with HaarPSI value 0.961 (see Table 2), but the image by the fastMRI-UNet is only 0.836. HaarPSI value of another part at soleus muscle by the fastMRI-UNet and our SENSE3d model are 0.906 and 0.970, respectively. Our model gives 0.064 higher than the fastMRI-UNet model. This case shows that our model is stable to reconstruct image and get nice results from the different data by different machine acquisition.

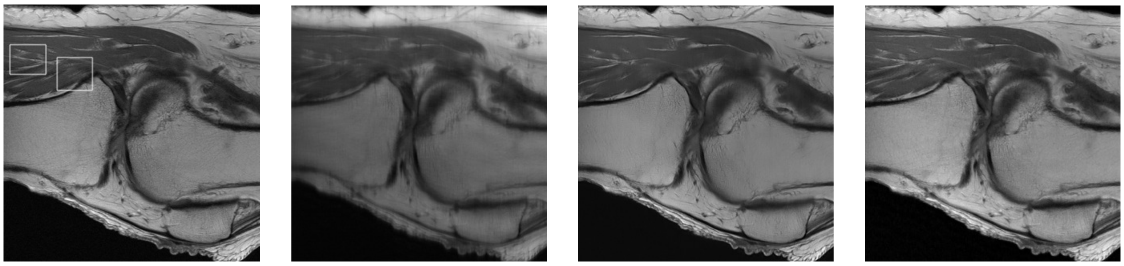

(a) Full SoS (b) SoS (35%) (c) fastMRI-UNet (d) *SENSE3d*

Figure 11. *MRI data with sampling model 770-35%-59 as shown in Fig. 8(b) with two to-be zoom-in rectangle areas. (a) Reference SoS image of 15 coil images by full K-space data with two zoom-in regions. (b) SoS image by 35% K-space data. (c) fastMRI-UNet. (d) Our* SENSE3d *model.*

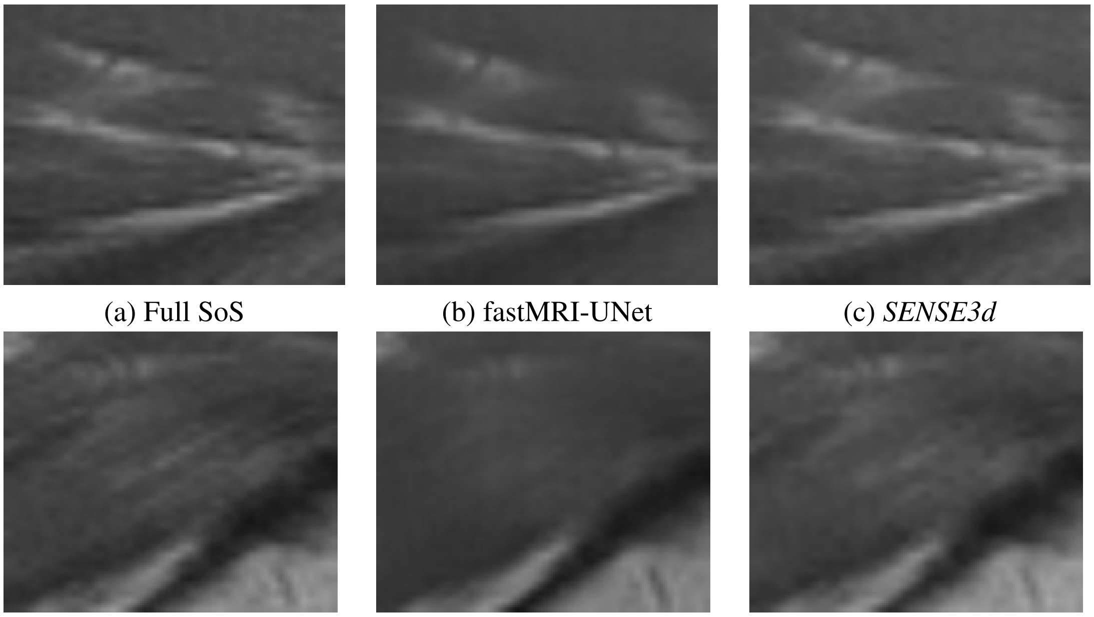

(a) Full SoS (b) fastMRI-UNet (c) *SENSE3d*

(d) Full SoS (e) fastMRI-UNet (f) *SENSE3d*

Figure 12. *Two zoom-in parts of Fig. 11 . (a)(d) Reference SoS image. (b)(e) fastMRI-UNet. (c)(f)* SENSE3d.

5. Conclusions and further remarks. We have proposed an effective *SENSE3d* model for the pMRI reconstruction. The proposed method can reconstruct high quality images from the sampled *K*-space data with a high acceleration rate by decoupling effects of the desired image (slice) and sensitivity maps. The developed *SENSE3d*-algorithm, which consists of a sequence of alternating

Slice-step and Sensitivity-step, exploits the decoupled slices and sensitivity maps. Each Slice-step solves a convex optimization problem for an estimated image with the given estimations of sensitivity maps while each Sensitivity-step solves an non-convex optimization problem for estimated sensitivity maps with the given estimation of the desired image. The convergence analysis for the optimization algorithm in both Slice-step and Sensitivity-step has been studied. Numerical results on various data and comparisons to other state-of-the-art methods including deep learning methods have demonstrated that the proposed method can produce images of high quality and reduce aliasing artifacts efficiently caused by inaccurate estimation of each coil sensitivity.

The using of neural networks is to learn the relationship between input data (*K*-space data) and output data (for example, slice images) by training data. Thus, the databases with a large number of multi-coil *K*-space data are needed to train the neural networks for pMRI reconstruction [18]. The challenge of pMRI reconstruction by using neural networks is their instability of predicting output data when the imaging conditions of input data are different with different training conditions [35]. How to take the advantages of our model to improve the performance of the models based on deep learning methods can be one of our future research topics.

6. Appendix.

6.1. Proof of Theorem 3.1. In this appendix, we give the proof of Theorem 3.1. To this end, we first introduce our notation and recall some necessary background materials from optimization. The class of all lower semicontinuous convex functions $f : \mathbb{C}^d \to (-\infty, +\infty]$ such that $\mathrm{dom}\ f := \{x \in \mathbb{C}^d : f(x) < +\infty\} \neq \emptyset$ is denoted by $\Gamma_0(\mathbb{C}^d)$. The indicator function of a closed convex set C in $\mathbb{C}^d$ is defined, at $u \in \mathbb{C}^d$, as

$$\iota_C(u) := \begin{cases} 0, & \text{if } u \in C, \\ +\infty, & \text{otherwise.} \end{cases}$$

Clearly, the indicator function ι_C is in $\Gamma_0(\mathbb{C}^d)$ for any closed nonempty convex set C.

For a function $f \in \Gamma_0(\mathbb{C}^d)$, the proximity operator of f with parameter λ, denoted by $\mathrm{prox}_{\lambda f}$, is a mapping from $\mathbb{C}^d$ to itself, defined for a given point $x \in \mathbb{C}^d$ by

$$\mathrm{prox}_{\lambda f}(x) := \mathrm{argmin}\left\{\frac{1}{2}\|u - x\|_2^2 + \lambda f(u) : u \in \mathbb{C}^d\right\}.$$

We also need the notation of conjugate. The conjugate of $f \in \Gamma_0(\mathbb{C}^d)$ is the function $f^* \in \Gamma_0(\mathbb{C}^d)$ defined at $x \in \mathbb{C}^d$ by $f^*(x) := \sup\{\langle u, x\rangle - f(u) : u \in \mathbb{C}^d\}$. A key property of the proximity operators of f and its conjugate is

$$\mathrm{prox}_{\lambda f}(x) + \lambda \mathrm{prox}_{\lambda^{-1} f^*}(x/\lambda) = x, \tag{6.1}$$

which holds for all $x \in \mathbb{C}^n$ and any $\lambda > 0$.

For a real function f defined on $\mathbb{C}^d$, we say f is Fréchet differentiable at $x \in \mathbb{C}^d$ if there exits a $v \in \mathbb{C}^d$ such that

$$\lim_{y \to x} \frac{|f(y) - f(x) - \langle v, y - x\rangle|}{\|y - x\|_2} = 0.$$

The vector v is called the gradient of f at x, denoted by $\nabla f(x)$. As an example, $\nabla(\|A \cdot -b\|_2^2) = A^\top(A \cdot -b)$, where $A \in \mathbb{C}^{d\times n}$ and $b \in \mathbb{C}^d$.

We consider the following optimization problem

$$\min_{x\in\mathbb{C}^n} p(x)+q(x)+r(Ax), \tag{6.2}$$

where A is a $d\times n$ matrix, $p\in\Gamma_0(\mathbb{C}^n)$ is differentiable, $q\in\Gamma_0(\mathbb{C}^n)$, and $r\in\Gamma_0(\mathbb{C}^d)$.

Several algorithms have been developed for the optimization problem (6.2), see, for example, [20, 39]. We adopt the algorithm given in [39] for problem (6.2) since it converges under a weaker condition and can choose a larger step-size, yielding a faster convergence. This algorithm, named as Primal-Dual Three-Operator splitting (PD3O), has the following iteration:

$$x^k = \mathrm{prox}_{\gamma q}(y^k) \tag{6.3a}$$

$$z^{k+1} = \mathrm{prox}_{\delta r^*}\left((I-\gamma\delta AA^\top)z^k+\delta A(2x^k-y^k-\gamma\nabla p(x^k))\right) \tag{6.3b}$$

$$y^{k+1} = x^k-\gamma\nabla p(x^k)-\gamma A^\top z^{k+1} \tag{6.3c}$$

One PD3O iteration can be viewed as an operator $\mathrm{T}_{\mathrm{PD3O}}$ such that $(y^{k+1},z^{k+1})=\mathrm{T}_{\mathrm{PD3O}}(y^k,z^k)$. The convergence analysis of PD3O is given in the following lemma.

Lemma 6.1 (Sublinear convergence rate [39]). *Let $p\in\Gamma_0(\mathbb{C}^n)$ and its gradient be Lipschitz continuous with constant ν. Choose γ and δ such that $\gamma<2/\nu$ and $B=\frac{\gamma}{\delta}(I-\gamma\delta AA^\top)$ is positive definite. Let (y^*,z^*) be any fixed point of $\mathrm{T}_{\mathrm{PD3O}}$, and $\{(y^k,z^k)\}_{k\geqslant 0}$ be the sequence generated by PD3O. Define $\|(y,z)\|_B := \sqrt{\|y\|^2+\langle z,Bz\rangle}$. Then, the following statements hold.*

(i) The sequence $\{(\|(y^k,z^k)-(y^*,z^*)\|_B)\}_{k\geqslant 0}$ is monotonically nonincreasing.

(ii) The sequence $\{(\|(y^{k+1},z^{k+1})-(y^k,z^k)\|_B)\}_{k\geqslant 0}$ is monotonically nonincreasing. Moreover,

$$\|(y^{k+1},z^{k+1})-(y^k,z^k)\|_B^2 = o\left(\frac{1}{k+1}\right).$$

We remark that the statements in Lemma 6.1 are originally presented in real vector space $\mathbb{R}^n$ (see [39]). By using the inner product (3.1) for $\mathbb{C}^n$, we essentially work with real vector space $\mathbb{R}^{2n}$. Therefore, the results in Lemma 6.1 hold on $\mathbb{C}^n$ as well.

By identifying p, q, r and A in (6.2), respectively, as follows

$$p(\cdot)=\frac{1}{2}\|M\cdot-g\|^2,\; q(\cdot)=\iota_{\mathbb{R}^n}(\cdot),\; r(\cdot)=\|\Gamma(\cdot+b)\|_1,\; A=WN \tag{6.4}$$

with $b=W(I_L\otimes F^{-1})g$, the PD3O algorithm can be applied for solving problem (3.3). To efficiently implement this algorithm, we need to know both prox_q and $\mathrm{prox}_{\delta r^*}$. By the definition of proximity operator, $\mathrm{prox}_q=\mathrm{Re}$, i.e., prox_q takes the real part of an input. The proximity operator $\mathrm{prox}_{\delta r^*}$ is given in the next lemma.

Lemma 6.2. *Let r be given in (6.4). Then, for $\delta>0$ and $z\in\mathbb{C}^d$, $\mathrm{prox}_{\delta r^*}(z)=(z+\delta b)-\mathrm{prox}_{\|\Gamma\cdot\|_1}(z+\delta b)$.*

Proof. Write $w=\mathrm{prox}_{\delta r^*}(z)$. From the identity (6.1), $w=z-\delta\mathrm{prox}_{\delta^{-1}r}(\delta^{-1}z)$. Based on the separable property of r in (6.4), that is, $r(u)=\|\Gamma(u+b)\|_1=\sum_{k=1}^d\gamma[k]|u[k]+b[k]|$, we have that $w[k]=z[k]-\delta\mathrm{prox}_{\delta^{-1}\gamma[k]|\cdot+b[k]|}(\delta^{-1}z[k])$, for $k=1,2,\ldots,d$. By a simple manipulation on the above proximity operator, we have that $w[k]=(z[k]+\delta b[k])-\mathrm{prox}_{\gamma[k]|\cdot|}(z[k]+\delta b[k])$. This completes the proof of this result. ∎

The proximity operator $\mathrm{prox}_{\|\Gamma\cdot\|_1}$ is the well-known soft shrinkage operator $\mathrm{soft}(x, \Gamma)$. To show the convergence of the PD3O algorithm under the proper choices of parameters γ and δ, we need the following lemma.

Lemma 6.3. *Let M and g be given in (1.2), and let p and A be given in (6.4). Then, the following statements hold:*
(i). The gradient of p is κ-Lipschitz continuous, where κ is given in (3.4).
(ii). For any positive numbers γ and δ, the matrix $I - \gamma\delta AA^\top$ is positive definite if and only if $\gamma\delta < 1/\kappa$.

Proof. Item (i): Note that $\nabla p(u) = M^\top(Mu - g)$. Then, ∇p is $\|M\|^2$-Lipschitz continuous. Define $Q = \overline{\sum_{\ell=1}^L s_\ell s_\ell^\top}$ which is the entry-wise conjugate of the matrix $\sum_{\ell=1}^L s_\ell s_\ell^\top$. From (1.2), we have $M^\top M = \sum_{\ell=1}^L \mathrm{diag}(\bar{s}_\ell) F^\top P F S_\ell = (F^\top P F) \odot Q$. Since Q is positive semi-definite matrix, we have, for example, by Theorem 5.5.18 in [13], that $\|M^\top M\|_2 \leqslant \max_{i,j} |Q[i,j]| \|F^\top P F\|_2$. Further, due to $\|F^\top P F\| \leqslant 1$, $\max_{i,j} |Q[i,j]| = \max_k |Q[k,k]|$, and $Q[k,k] = \sum_{\ell=1}^L |s_\ell[k]|^2$, we have $\|M^\top M\|_2 \leqslant \kappa$.

Item (ii): The proof replies on the estimation of the norm of $AA^\top$. From $A = WN$ and $W^\top W = I$, one has $\|AA^\top\|_2 = \|A^\top A\|_2 = \|N^\top N\|_2$. Similar to the discussion in Item (i), we have $N^\top N = (F^\top(I-P)F) \odot Q$ and $\|N^\top N\|_2 \leqslant \kappa$. Therefore, the largest eigenvalue of $AA^\top$ is less than κ. As a result, $I - \gamma\delta AA^\top$ is positive definite if and only if $\gamma\delta < 1/\kappa$. This completes the proof. ■

Proof. (Theorem 3.1) By Lemma 6.3, the gradient p in (6.4) is κ-Lipschitz continuous and the matrix B is positive definite if and only if $\gamma\delta < 1/\kappa$, the result of this theorem follows immediately from Lemma 6.1. ■

6.2. Proof of Theorem 3.2. For given P_{sel}, M, g_{est}, Γ and W in (3.10), define

$$h(s) := \frac{1}{2}\|P_{sel}(Qs - g_{est})\|_2^2 + \frac{1}{2}\|\Gamma W s\|_2^2. \tag{6.5}$$

We have the following result for the function h.

Lemma 6.4. *Let h be defined in (6.5). Then, the gradient of h is Lipschitz continuous with Lipschitz constant $\|u\|_\infty^2 + \|\mathrm{diag}(\Gamma)\|_\infty^2$.*

Proof. Note that $\nabla h(s) = Q^\top P_{sel}(Qs - g_{est}) + W^\top \Gamma^2 W s$. For any vectors s_1 and s_2, we have $\|\nabla h(s_1) - \nabla h(s_2)\|_2 = \|(Q^\top P_{sel} Q + W^\top \Gamma^2 W)(s_1 - s_2)\|_2 \leqslant (\|Q\|_2^2 \|P_{sel}\|_2 + \|W\|_2^2 \|\Gamma\|_2^2)\|s_1 - s_2\|_2$. We know that $\|P_{sel}\|_2 = 1$, $\|W^\top\|_2 = 1$, and $\|\Gamma\|_2 = \|\mathrm{diag}(\Gamma)\|_\infty$. Next we estimate the norm of Q. Since

$$\begin{aligned} Q^\top Q &= (I_L \otimes (F\mathrm{diag}(u)))^\top (I_L \otimes (F\mathrm{diag}(u))) \\ &= (I_L \otimes (\mathrm{diag}(u) F^{-1}))(I_L \otimes (F\mathrm{diag}(u))) \\ &= I_L \otimes (\mathrm{diag}(u)\mathrm{diag}(u))), \end{aligned}$$

we have that $\|Q\|_2^2 = \|Q^\top Q\|_2 = \|I_L \otimes (\mathrm{diag}(u)\mathrm{diag}(u))\|_2 = \|\mathrm{diag}(u)\|_2^2 = \|u\|_\infty^2$. Hence, the gradient of h is Lipschitz continuous with Lipschitz constant $\|u\|_\infty^2 + \|\mathrm{diag}(\Gamma)\|_\infty^2$. ■

Proof. (Theorem 3.2) Note that $h(s)$ is a quadratic polynomial with respect to s and the set D given in (3.9) is determined by a set of polynomials. Then, $h(s) + \iota_D(s)$ is a Kurdyka-Łojasiewicz function (see, e.g., [1]). Hence, the result is the direct consequence of Theorem 5.3 of [1]. ■

REFERENCES

[1] H. Attouch, J. Bolte, and B. Svaiter, *Convergence of descent methods for semi-algebraic and tame problems: proximal algorithms, forward-backward splitting, and regularized Gauss-Seidel methods*, Mathematical Programming, Ser. A, 137 (2013), pp. 91–129.

[2] M. Blaimer, F. Breuer, M. Mueller, R. M. Heidemann, M. A. Griswold, and P. M. Jakob, *SMASH, SENSE, PILS, GRAPPA: how to choose the optimal method*, Topics in Magnetic Resonance Imaging, 15 (2004), pp. 223–236.

[3] J.-F. Cai, J. K. Choi, and K. Wei, *Data driven tight frame for compressed sensing MRI reconstruction via off-the-grid regularization*, SIAM Journal on Imaging Sciences, 13 (2020), pp. 1272–1301.

[4] L. Chaâri, J. C. Pesquet, A. Benazza-Benyahia, and P. Ciuciu, *A wavelet-based regularized reconstruction algorithm for SENSE parallel MRI with applications to neuroimaging*, Medical Image Analysis, 12 (2011), pp. 185–201.

[5] I. Y. Chun, B. Adcock, and T. M. Talavage, *Efficient compressed sensing SENSE pMRI reconstruction with joint sparsity promotion*, IEEE Transactions on Medical Imaging, 35 (2016), pp. 354–368.

[6] M. Doneva, *Mathematical models for magnetic resonance imaging reconstruction: an overview of the approaches, problems, and future research areas*, IEEE Signal Processing Magazine, 37 (2020), pp. 24–32.

[7] W. A. Edelstein, J. M. Hutchison, G. Johnson, and T. Redpath, *Spin warp NMR imaging and applications to human whole-body imaging*, Physics in medicine & biology, 25 (1980), p. 751.

[8] S. G. Finlayson, J. D. Bowers, J. Ito, J. L. Zittrain, A. L. Beam, and I. S. Kohane, *Adversarial attacks on medical machine learning*, Science, 363 (2019), pp. 1287–1289.

[9] M. A. Griswold, P. M. Jakob, R. M. Heidemann, M. Nittka, V. Jellus, J. Wang, B. Kiefer, and A. Haase, *Generalized autocalibrating partially parallel acquisitions (GRAPPA)*, Magnetic Resonance in Medicine, 47 (2002), pp. 1202–1210.

[10] J. P. Haldar and J. Zhuo, *P-LORAKS: low-rank modeling of local k-space neighborhoods with parallel imaging data*, Magnetic Resonance in Medicine, 75 (2016), pp. 1499–1514.

[11] B. Han, *Framelets and Wavelets: Algorithms, Analysis, and Applications*, Springer International Publishing, 2018.

[12] B. Han, T. Li, and X. Zhuang, *Directional compactly supported box spline tight framelets with simple geometric structure*, Applied Mathematics Letters, 91 (2019).

[13] R. Horn and C.Johnson, *Topics in matrix analysis*, Cambridge University Press, 1991.

[14] M. Jacob, M. P. Mani, and J. C. Ye, *Structured low-rank algorithms: theory, magnetic resonance applications, and links to machine learning*, IEEE Signal Processing Magazine, 37 (2020), pp. 54–68.

[15] K. H. Jin, D. Lee, and J. C. Ye, *A general framework for compressed sensing and parallel MRI using annihilating filter based low-rank hankel matrix*, IEEE Transactions on Computational Imaging, 2 (2016), pp. 480–495.

[16] K. H. Jin, M. T. McCann, E. Froustey, and M. Unser, *Deep convolutional neural network for inverse problems in imaging*, IEEE Transactions on Image Processing, 26 (2017), pp. 4509–4522.

[17] F. Knoll, C. Clason, K. Bredies, M. Uecker, and R. Stollberger, *Parallel imaging with nonlinear reconstruction using variational penalties*, Magnetic Resonance in Medicine, 67 (2012), pp. 34–41.

[18] F. Knoll, K. Hammernik, C. Zhang, S. Moeller, T. Pock, D. K. Sodickson, and M. Akcakaya, *Deep-learning methods for parallel magnetic resonance image reconstruction: a survey of the current approaches, trends, and issues*, IEEE Signal Processing Magazine, 37 (2020), pp. 128–140.

[19] J. Li, H. Feng, and X. Zhuang, *Convolutional neural networks for spherical signal processing via area-regular spherical haar tight framelets*, IEEE Transactions on Neural Networks and Learning Systems, (2022).

[20] Q. Li and N. Zhang, *Fast proximity-gradient algorithms for structured convex optimization problems*, Applied and Computational Harmonic Analysis, 41 (2016), pp. 491 – 517.

[21] Y.-R. Li, R. H. Chan, L. Shen, Y.-C. Hsu, and W.-Y. I. Tseng, *An adaptive directional haar framelet-based reconstruction algorithm for parallel magnetic resonance imaging*, SIAM Journal on Imaging Sciences, 9 (2016), pp. 794–821.

[22] Y.-R. Li, L. Shen, and X. Zhuang, *A tailor-made 3-dimensional directional haar semi-tight framelet for pMRI reconstruction*, Applied and Computational Harmonic Analysis, 60.

[23] Y.-R. Li and X. Zhuang, *Parallel magnetic resonance imaging reconstruction algorithm by 3-dimension directional Haar tight framelet regularization*, in SPIE Proc., San Diego, 2019, pp. 111381C–1–8.

[24] M. Lustig and J. M. Pauly, *SPIRiT:iterative self-consistent parallel imaging reconstruction from arbitrary k-space*, Magnetic Resonance in Medicine, 64 (2010), pp. 457–471.

[25] J. Lyu, U. Nakarmi, D. Liang, J. Sheng, and L. Ying, *Kernl: Kernel-based nonlinear approach to parallel MRI reconstruction*, IEEE Transactions on Medical Imaging, 38 (2019), pp. 312–321.
[26] M. J. Muckley, B. Riemenschneider, A. Radmanesh, S. Kim, G. Jeong, J. Ko, Y. Jun, H. Shin, D. Hwang, M. Mostapha, et al., *Results of the 2020 fastmri challenge for machine learning mr image reconstruction*, IEEE transactions on medical imaging, 40 (2021), pp. 2306–2317.
[27] M. Murphy, M. Alley, J. Demmel, K. Keutzer, S. Vasanawala, and M. Lustig, *Fast ℓ_1-SPIRiT compressed sensing parallel imaging MRI: Scalable parallel implementation and clinically feasible runtime*, IEEE Transactions on Medical Imaging, 31 (2012), pp. 1250–1262.
[28] K. P. Pruessmann, M. Weiger, M. B. Scheidegger, and P. Boesiger, *SENSE: sensitivity encoding for fast MRI*, Magnetic Resonance in Medicine, 42 (1999), pp. 952–962.
[29] G. K. Rafael Reisenhofer, Sebastian Bosse and T. Wiegand, *A haar wavelet-based perceptual similarity index for image quality assessment*, Signal Processing: Image Communication, 61 (2018), pp. 33–43.
[30] O. Ronneberger, P. Fischer, and T. Brox, *U-net: Convolutional networks for biomedical image segmentation*, in Medical Image Computing and Computer-Assisted Intervention–MICCAI 2015: 18th International Conference, Munich, Germany, October 5-9, 2015, Proceedings, Part III 18, Springer, 2015, pp. 234–241.
[31] P. J. Shin, P. E. Z. Larson, M. A. Ohliger, M. Elad, J. M. Pauly, and a. M. L. Daniel B. Vigneron, *Calibrationless parallel imaging reconstruction based on structured low-rank matrix completion*, Magnetic Resonance in Medicine, 725 (2014), pp. 959–970.
[32] A. Sriram, J. Zbontar, T. Murrell, A. Defazio, C. L. Zitnick, N. Yakubova, F. Knoll, and P. Johnson, *End-to-end variational networks for accelerated mri reconstruction*, in Medical Image Computing and Computer Assisted Intervention–MICCAI 2020: 23rd International Conference, Lima, Peru, October 4–8, 2020, Proceedings, Part II 23, Springer, 2020, pp. 64–73.
[33] M. Uecker, P. Lai, M. J. Murphy, P. Virtue, M. Elad, J. M. Pauly, S. S. Vasanawala, and M. Lustig, *ESPIRiT-an eigenvalue approach to autocalibrating parallel MRI: where SENSE meets GRAPPA*, Magnetic Resonance in Medicine, 71 (2014), pp. 990–1001.
[34] M. Uecker and M. Lustig, *Estimating absolute-phase maps using espirit and virtual conjugate coils*, Magnetic Resonance in Medicine, 77 (2017), pp. 1201–1207.
[35] C. P. B. A. V. Antun, F. Renna and A. C. Hansen, *On instabilities of deep learning in image reconstruction and the potential costs of ai*, Proceedings of the National Academy of Sciences, 117 (2020), pp. 30088–30095.
[36] S. Wang, S. Tan, Y. Gao, Q. Liu, L. Ying, T. Xiao, Y. Liu, X. Liu, H. Zheng, and D. Liang, *Learning joint-sparse codes for calibration-free parallel MR imaging*, IEEE Transactions on Medical Imaging, 37 (2018), pp. 251–261.
[37] D. S. Weller, J. R. Polimeni, L. Grady, L. L. Wald, E. Adalsteinsson, and V. K. Goyal, *Sparsity-promoting calibration for GRAPPA accelerated parallel MRI reconstruction*, IEEE Transactions on Medical Imaging, 32 (2013), pp. 1325–1335.
[38] Y. Xiao and X. Zhuang, *Adaptive directional haar tight framelets on bounded domains for digraph signal representations*, Journal of Fourier Analysis and Applications, 27 (2021), pp. 1–26.
[39] M. Yan, *A new primal-dual algorithm for minimizing the sum of three functions with a linear operator*, Journal of Scientific Computing, 76 (2018), pp. 1698–1717.
[40] G. Yang, S. Yu, H. Dong, G. Slabaugh, P. L. Dragotti, X. Ye, F. Liu, S. Arridge, J. Keegan, Y. Guo, and D. Firmin, *Dagan: Deep de-aliasing generative adversarial networks for fast compressed sensing MRI reconstruction*, IEEE Transactions on Medical Imaging, 37 (2017), pp. 1310–1321.
[41] Y. Yang, J. Sun, H. Li, and Z. Xu, *Deep ADMM-Net for compressive sensing MRI*, in Proceedings of the 30th International Conference on Neural Information Processing Systems, 2016, pp. 10–18.
[42] M. Yashtini, *Euler's elastica-based algorithm for parallel MRI reconstruction using SENSitivity encoding*, Optimization Letters, 14 (2020), pp. 1435–1458.
[43] X. Ye, Y. Chen, and F. Huang, *Computational acceleration for MR image reconstruction in partially parallel imaging*, IEEE Transactions on Medical Imaging, 30 (2011), pp. 1055–1063.
[44] L. Ying and J. Sheng, *Joint image reconstruction and sensitivity estimation in SENSE (JSENSE)*, Magnetic Resonance in Medicine, 57 (2007), pp. 1196–1202.
[45] J. Zbontar, F. Knoll, A. Sriram, T. Murrell, Z. Huang, M. J. Muckley, A. Defazio, R. Stern, P. Johnson, M. Bruno, et al., *fastMRI: An open dataset and benchmarks for accelerated MRI*, arXiv preprint arXiv:1811.08839, (2018).